SANDIA REPORT

SAND2010-6218
Unlimited Release
Printed September, 2010

Development, Sensitivity Analysis, and Uncertainty Quantification of High-Fidelity Arctic Sea Ice Models

Kara Peterson, Pavel Bochev, Biliana Paskaleva

Prepared by
Sandia National Laboratories
Albuquerque, New Mexico 87185 and Livermore, California 94550

Sandia National Laboratories is a multi-program laboratory managed and operated by Sandia Corporation, a wholly owned subsidiary of Lockheed Martin Corporation, for the U.S. Department of Energy's National Nuclear Security Administration under contract DE-AC04-94AL85000.

Sandia National Laboratories

Issued by Sandia National Laboratories, operated for the United States Department of Energy by Sandia Corporation.

Available to DOE and DOE contractors from
U.S. Department of Energy
Office of Scientific and Technical Information
P.O. Box 62
Oak Ridge, TN 37831

Telephone: (865) 576-8401
Facsimile: (865) 576-5728
E-Mail: reports@adonis.osti.gov
Online ordering: http://www.osti.gov/bridge

Available to the public from
U.S. Department of Commerce
National Technical Information Service
5285 Port Royal Rd
Springfield, VA 22161

Telephone: (800) 553-6847
Facsimile: (703) 605-6900
E-Mail: orders@ntis.fedworld.gov
Online ordering: http://www.ntis.gov/help/ordermethods.asp?loc=7-4-0#online

SAND2010-6218
Unlimited Release
Printed September, 2010

Development, Sensitivity Analysis, and Uncertainty Quantification of High-Fidelity Arctic Sea Ice Models

Kara Peterson
Applied Mathematics and Applications, MS-1318
Sandia National Laboratories
Albuquerque, NM 87185-1320
kjpeter@sandia.gov

Pavel Bochev
Applied Mathematics and Applications, MS-1320
Sandia National Laboratories
Albuquerque, NM 87185-1320
pbboche@sandia.gov

Biliana Paskaleva
Software Engineering and Quality Environments, MS-1138
Sandia National Laboratories
Albuquerque, NM 87185-1081
bspaska@sandia.gov

Abstract

Arctic sea ice is an important component of the global climate system and due to feedback effects the Arctic ice cover is changing rapidly. Predictive mathematical models are of paramount importance for accurate estimates of the future ice trajectory. However, the sea ice components of Global Climate Models (GCMs) vary significantly in their prediction

of the future state of Arctic sea ice and have generally underestimated the rate of decline in minimum sea ice extent seen over the past thirty years. One of the contributing factors to this variability is the sensitivity of the sea ice to model physical parameters.

A new sea ice model that has the potential to improve sea ice predictions incorporates an anisotropic elastic-decohesive rheology and dynamics solved using the material-point method (MPM), which combines Lagrangian particles for advection with a background grid for gradient computations. We evaluate the variability of the Los Alamos National Laboratory CICE code and the MPM sea ice code for a single year simulation of the Arctic basin using consistent ocean and atmospheric forcing. Sensitivities of ice volume, ice area, ice extent, root mean square (RMS) ice speed, central Arctic ice thickness, and central Arctic ice speed with respect to ten different dynamic and thermodynamic parameters are evaluated both individually and in combination using the Design Analysis Kit for Optimization and Terascale Applications (DAKOTA). We find similar responses for the two codes and some interesting seasonal variability in the strength of the parameters on the solution.

Acknowledgment

Funding from Laboratory Directed Research and Development program is gratefully acknowledged. The authors would like to thank Elizabeth Hunke for valuable advice on the CICE code and Denis Ridzal for helpful discussions regarding sensitivity and uncertainty analyses.

Contents

Nomenclature **12**

1 Introduction **15**

2 Governing Equations **19**

2.1 Dynamics 19

2.2 Ice Thickness Distribution 20

2.3 Thermodynamics 21

3 Simulations **25**

3.1 Model Configurations 25

3.2 External Forcing 27

3.3 Results for Nominal Simulation 27

4 Sensitivity Analysis **31**

4.1 Parameter Selection 31

4.2 Methodology 33

4.2.1 Background 33

4.2.2 Linear regression model 34

4.2.3 Application to sea-ice models 36

4.3 Single Parameter Sensitivity Results 37

4.4 Multi-Parameter Sensitivity Results 38

5 Conclusions **61**

References **63**

List of Figures

3.1.1 The ice thickness distribution used in both the MPM and CICE calculations for regions where ice is initially assumed to exist. 26

3.1.2 The computational domain for the pan-Arctic calculation (land regions in red) showing initial average thickness for (a) the MPM calculation and (b) the CICE calculation. 26

3.3.1 The ice thickness in meters for (a) the MPM calculation at the end of September, (b) the MPM calculation at the end of December, (c) the CICE calculation at the end of September, (d) the CICE calculation at the end of December. 28

3.3.2 The ice velocity for (a) the MPM calculation at the end of September, (b) the MPM calculation at the end of December, (c) the CICE calculation at the end of September, (d) the CICE calculation at the end of December. 29

4.3.1 Normalized sensitivity of total ice area with respect to (a) visual ice albedo, (b) near-infrared ice albedo, (c) visual snow albedo, (d) emissivity, (e) fraction of shortwave absorbed by ice, (f) fresh ice conductivity, (g) maximum salinity, (h) ice-ocean drag coefficient, (i) ridging parameter a^*, and (j) ridging parameter μ. (MPM curve in red and CICE curve in blue.) 39

4.3.2 Standardized regresion coefficients for total ice extent with respect to (a) visual ice albedo, (b) near-infrared ice albedo, (c) visual snow albedo, (d) emissivity, (e) fraction of shortwave absorbed by ice, (f) fresh ice conductivity, (g) maximum salinity, (h) ice-ocean drag coefficient, (i) ridging parameter a^*, and (j) ridging parameter μ. (MPM curve in red and CICE curve in blue.) . . 40

4.3.3 Standardized regression coefficients for total ice volume with respect to (a) visual ice albedo, (b) near-infrared ice albedo, (c) visual snow albedo, (d) emissivity, (e) fraction of shortwave absorbed by ice, (f) fresh ice conductivity, (g) maximum salinity, (h) ice-ocean drag coefficient, (i) ridging parameter a^*, and (j) ridging parameter μ. (MPM curve in red and CICE curve in blue.) . . 41

4.3.4 Standardized regression coefficients for RMS ice speed with respect to (a) visual ice albedo, (b) near-infrared ice albedo, (c) visual snow albedo, (d) emissivity, (e) fraction of shortwave absorbed by ice, (f) fresh ice conductivity, (g) maximum salinity, (h) ice-ocean drag coefficient, (i) ridging parameter a^*, and (j) ridging parameter μ. (MPM curve in red and CICE curve in blue.) . . 42

4.3.5 Standardized regression coefficients for central Arctic ice thickness with respect to (a) visual ice albedo, (b) near-infrared ice albedo, (c) visual snow albedo, (d) emissivity, (e) fraction of shortwave absorbed by ice, (f) fresh ice conductivity, (g) maximum salinity, (h) ice-ocean drag coefficient, (i) ridging parameter a^*, and (j) ridging parameter μ. (MPM curve in red and CICE curve in blue.) 43

4.3.6 Standardized regression coefficients for central Arctic ice speed with respect to (a) visual ice albedo, (b) near-infrared ice albedo, (c) visual snow albedo, (d) emissivity, (e) fraction of shortwave absorbed by ice, (f) fresh ice conductivity, (g) maximum salinity, (h) ice-ocean drag coefficient, (i) ridging parameter a^*, and (j) ridging parameter μ. (MPM curve in red and CICE curve in blue.) . . 44

4.4.1 Standardized regression coefficients for total ice area with respect to the ten parameters for (a) MPM and (b) CICE. 46

4.4.2 Standardized regression coefficients for total ice extent with respect to the ten parameters for (a) MPM and (b) CICE. 47

4.4.3 Standardized regression coefficients for total ice volume with respect to the ten parameters for (a) MPM and (b) CICE. 48

4.4.4 Standardized regression coefficients for RMS ice speed with respect to the ten parameters for (a) MPM and (b) CICE. 49

4.4.5 Standardized regression coefficients for central Arctic ice thickness with respect to the ten parameters for (a) MPM and (b) CICE. 50

4.4.6 Standardized regression coefficients for central Arctic ice speed with respect to the ten parameters for (a) MPM and (b) CICE. 52

4.4.7 The seasonal cycle showing the mean (black) and two-sigma bounds (blue) of (a) MPM ice volume, (b) CICE ice volume, (c) MPM ice area, (d) CICE ice area, (e) MPM RMS ice speed, (f) CICE RMS ice speed, for 50 Latin hypercube samples. 59

List of Tables

4.1.1 Model Parameters for Sensitivity Analysis. 31

4.1.2 Response Functions for Sensitivity Analysis. 32

4.4.1 Three most significant parameters in CICE and MPM for A_{tot} ranked according to the magnitude of the standardized regression coefficient (in parentheses) for each month. 51

4.4.2 Three most significant parameters in CICE and MPM for E_{tot} ranked according to the magnitude of the standardized regression coefficient (in parentheses) for each month. 53

4.4.3 Three most significant parameters in CICE and MPM for V_{tot} ranked according to the magnitude of the standardized regression coefficient (in parentheses) for each month. 54

4.4.4 Three most significant parameters in CICE and MPM for $\mathbf{v}_{rms}$ ranked according to the magnitude of the standardized regression coefficient (in parentheses) for each month. 55

4.4.5 Three most significant parameters in CICE and MPM for h_{CA} ranked according to the magnitude of the standardized regression coefficient (in parentheses) for each month. 56

4.4.6 Three most significant parameters in CICE and MPM for $\mathbf{v}_{CA}$ ranked according to the magnitude of the standardized regression coefficient (in parentheses) for each month. 57

Nomenclature

ρ - ice density

$\mathbf{v}$ - ice velocity

$\bar{h}$ - average ice thickness

$\boldsymbol{\sigma}$ - Cauchy stress tensor

$\boldsymbol{\tau}_a$ - atmospheric drag

ρ_a - air density

c_a - air drag coefficient

$\mathbf{v}_a$ - air velocity

$\boldsymbol{\tau}_w$ - ocean drag

ρ_w - ocean density

$\mathbf{v}_w$ - ocean velocity

c_w - ice-ocean drag coefficient

$\mathbf{f}_c$ - Coriolis force

$\mathbf{g}$ - acceleration due to gravity

ω - Earth's rotation

ϕ - latitude

H - sea surface height

g - ice thickness distribution

g_n - fractional area of ice in thickness category n

v_n - fractional volume of ice in thickness category n

G_n - discrete cumulative distribution function for thickness category n

ψ - ridging function

a^* - ridging parameter

μ - ridging parameter

T - temperature

T_0 - temperature at top of the ice

T_a - air temperature

k - conductivity

k_0 - conductivity of fresh ice

c - specific heat

c_0 - specific heat of fresh ice

S - salinity

S_{max} - maximum salinity at bottom of ice column

q - enthalpy

ϵ - emissivity

κ - extinction coefficient

i_0 - fraction of short wave radiation that is absorbed by ice

F_{SW} - short wave flux

F_{LW} - long wave flux

F_{lh} - flux of latent heat

F_{sh} - flux of sensible heat

$\alpha_{ice,v}$ - visual ice albedo

$\alpha_{ice,i}$ - near-infrared ice albedo

$\alpha_{snow,v}$ - visual snow albedo

$\alpha_{snow,i}$ - near-infrared snow albedo

α_{ocean} - ocean albedo

Chapter 1

Introduction

Arctic sea ice is an important component of the global climate system [3, 6]. It reflects a significant amount of solar radiation, insulates the ocean from the atmosphere, and influences ocean circulation by modifying the salinity of the upper ocean. Due to feedback effects, changes in the Arctic sea ice cover are accelerating [30]. Predictive mathematical models are essential for accurate estimates of the future ice trajectory. However, sea ice components of Global Climate Models (GCMs) vary greatly in their predictions for the future state of Arctic sea ice and have all underestimated the rate of decline in minimum sea ice extent over the last thirty years [32]. Additionally, the dynamic predictions of sea ice models differ substantially from model to model [17]. An important component of this variability is the sensitivity to model physical parameters. Therefore, understanding the sensitivity of the model outputs to various physical parameters is needed to further increase their accuracy and deliver predictive estimates of the future evolution of arctic sea ice. The aim of this research is to improve sea ice modeling predictions by both working on the development of a new high-resolution sea ice model that incorporates improved dynamics and alternative numerical techniques and evaluating the sensitivity of this model to perturbations in input parameters.

Sea ice is composed of a series of floes or large sections of intact ice separated by water or thin ice. It is mechanically driven by surface winds and ocean currents, which can result in cracks that expose open water or pressure ridges formed under convergence. Additionally, sea ice grows and melts seasonally in response to incoming solar radiation, thermal radiation from the atmosphere, and heat flux from the ocean. A complete sea ice model must incorporate variations in ice thickness including ridges and open water in leads, the annual cycle of growth and melt due to radiative forcing, and the mechanical deformation due to surface winds, ocean currents, and Coriolis forces. The main variables that must be solved for in a sea ice simulation are the spatially and temporally varying ice velocity and ice thickness.

Current state-of-the-art sea ice models have limitations in particular in the rheologies used to determine ice internal forces and in the numerical methods used to model advection. The typical rheology used for sea ice modeling is an isotropic viscous-plastic model. However, satellite data indicate that sea ice deformation is focused into narrow linear bands and overall the ice behaves anisotropically [5]. In addition, sea ice models are typically solved in an Eulerian frame and, therefore, the solving an advection equation results in artificial diffusion. We attempt to address these limitations in new model of sea ice [34]. We use an

elastic-decohesive rheology, which explicitly models the formation and evolution of cracks in the ice and is inherently anisotropic [29]. Numerical improvements come through solving the dynamics equations using the material-point method (MPM), which combines Lagrangian material points with a fixed background grid [33, 36]. The Lagrangian particles handle advection in a more natural way and tend to introduce less numerical diffusion. In this analysis, the MPM-elastic-decohesive model is compared with the Los Alamos National Laboratory (LANL) CICE code version 4.0 [14], which is a state-of-the-art sea ice model that is incorporated into the Community Earth System Model (CESM).

A number of authors have previously evaluated sea ice model sensitivities with the purpose of improving the models through parameter tuning. Holland *et al.* [10] calculated sensitivities of a dynamic-thermodynamic sea ice model to numerical conditions including time step and boundary conditions, parameter values such as albedo and drag coefficients, and physical processes such as ice rheology. The results displayed variation over the parameter space, however, the overall conclusion was that the model solution is robust to most perturbations. Chapman *et al.* [4] varied thirteen parameters of a dynamic-thermodynamic sea ice model simultaneously to gauge the sensitivity interdependencies concluding that many parameters are, in fact, interdependent.

More recently, Miller *et al.* [25] tuned the LANL CICE code by varying three parameters: the air-ice drag coefficient, an ice strength parameter, and the albedo of cold ice. They then matched observational data for the sea ice extent, velocity, and thickness. Kim *et al.* [16] used automatic differentiation implemented within CICE to determine parameters with the highest sensitivities. In this study they found that parameters other than albedo, such as ice conductivity were important. A selection of the important parameters from the Kim *et al.* study were considered in more detail in a paper by Hunke [11] that addressed the sensitivity of sea ice thickness.

Although, it is important to understand the sensitivity to changes in various physical parameters used in the code, it should be noted that other processes can have considerable effect on the solution. Miller *et al.* [24] and Hunke and Holland [13] found that variations in external (ocean and atmospheric) forcing are, unsurprisingly, very important and Losch *et al.* [22] found that numerical methods used in the solution of the governing equations also have a significant impact.

In this analysis we focus on the physical parameters within the model keeping the external forcing constant. This work builds on the previous studies by systematically comparing two codes with different physical and numerical components and incorporating more rigorous statistical analysis with the Design Analysis Kit for Optimization and Terascale Applications (DAKOTA) [1]. In this report the two sea ice models are run for one year in the Arctic basin. Sensitivities in volume, area, thickness, and velocity are calculated by varying ten parameters found in both the models.

The next section provides an overview of the sea ice governing equations with a focus on the aspects of the equations that contain parameters used in the sensitivity analysis. In Section 3 a description of the pan-Arctic calculation used in the sensitivity analysis and

a summary of the numerical implementation of each code is given. Section 4 includes a description of the sensitivity analysis and a discussion of the results. Conclusions are then given in Section 5.

Chapter 2

Governing Equations

As discussed in the introduction sea ice models must incorporate the dynamic deformation due to atmospheric winds, ocean currents and Coriolis forces, variations in the distribution of ice thickness, and seasonal thermodynamic growth and melt of the ice in order to solve for the spatial and temporally varying ice velocity and thickness. The following sections describe the governing equations for the ice velocity (2.1), the ice thickness distribution (2.2), and the thermodynamic change in ice thickness (2.3).

2.1 Dynamics

A conservation of linear momentum equation is solved to determine the sea ice velocity. Due to the large extent to thickness ratio of sea ice, a shallow ice formulation is used, which is derived by integrating the full three-dimensional sea ice momentum equation over the thickness and making suitable assumptions [7, 9]. Using this formulation the equation for two-dimensional ice velocity ($\mathbf{v}$) as a function of the average ice thickness at a point ($\bar{h}$) has the following form

$$\rho\bar{h}\frac{d\mathbf{v}}{dt} = \nabla\cdot(\bar{h}\boldsymbol{\sigma}) + \mathbf{t}_a + \mathbf{t}_w - \mathbf{f}_c - \rho\bar{h}\mathbf{g}\nabla H. \tag{2.1.1}$$

Note that d/dt here represents the material derivative, $\partial/\partial t + \mathbf{v}\cdot\nabla$. External forces acting on the ice include the atmospheric drag ($\mathbf{t}_a$), the ocean drag ($\mathbf{t}_w$), the Coriolis force ($\mathbf{f}_c$), and a sea surface tilt force ($\rho\bar{h}\mathbf{g}\nabla H$). In the case of the calculations presented here the sea surface tilt effect, which is a lower-order term, is neglected. The Coriolis force depends on the rotation of the Earth (ω) and the latitude (ϕ) in the following form

$$\mathbf{f}_c = 2\rho\bar{h}\omega\sin\phi(\mathbf{e}_3\times\mathbf{v}) \tag{2.1.2}$$

where $\mathbf{e}_e$ is the unit vector in the vertical direction. A quadratic drag law (Equation 2.1.3) is typically used for the ocean drag term. Here ρ_w is the ocean density, $\mathbf{v}_w$ is the two-dimensional ocean velocity, and c_w is the ocean drag coefficient that is taken as one of the sensitivity parameters for the analysis.

$$\boldsymbol{\tau_w} = c_w\rho_w\|\mathbf{v}-\mathbf{v}_w\|(\mathbf{v}-\mathbf{v}_w). \tag{2.1.3}$$

In the MPM sea ice code a quadratic drag law is also used for the atmospheric drag term (Equation 2.1.4), and similar to the ocean drag depends on the atmospheric density (ρ_a),

the wind velocity ($\mathbf{v}_a$), and an atmospheric drag coefficient (c_a).

$$\boldsymbol{\tau_a} = c_a \rho_a \|\mathbf{v}_a\| \mathbf{v}_a. \tag{2.1.4}$$

The CICE code, however, has an atmospheric boundary layer routine where the atmospheric drag is calculated based on turbulent scales for the velocity [14]. Therefore, the atmospheric drag coefficient was not chosen as a sensitivity parameter for this study.

The internal force term ($\nabla \cdot \bar{h}\boldsymbol{\sigma}$) depends on the stress tensor ($\boldsymbol{\sigma}$), which is obtained from the rheology or constitutive relation that relates stress to strain or strain rate. Most sea ice models use variations on the viscous-plastic constitutive model developed by Hibler [9]. CICE uses an elastic-viscous-plastic rheology, which is a modification of the viscous-plastic rheology that incorporates a non-physical elasticity for regularization purposes [12]. In the MPM sea ice model an elastic-decohesive rheology is used, which incorporates displacement discontinuities that corresponds to cracks in the ice [29]. Details of each of these rheologies can be found in the references, but will not be discussed in detail here since parameters from the distinct constitutive models are not used in the sensitivity analysis.

2.2 Ice Thickness Distribution

Variations in thickness are incorporated through a subgridscale ice thickness distribution [37]. The evolution equation for ice thickness is shown in Equation 2.2.1, where f is the rate of change in thickness due to thermodynamic effects and ψ is the ridging redistribution function. The thickness distribution evolves in time due to horizontal transport ($(\nabla \cdot \mathbf{v})g$), transport in thickness space ($\partial(fg)/\partial h$), and redstribution of thin ice to thicker ice in the ridging process (ψ).

$$\frac{dg}{dt} + (\nabla \cdot \mathbf{v})g + \frac{\partial(fg)}{\partial h} = \psi. \tag{2.2.1}$$

The ice thickness distribution (g) is analogous to a probability distribution and when integrated over thickness space is equal to one. Numerically, discrete thickness bins are used to define fractional areas that approximate the distribution. If the limits of the nth thickness bin are H_{n-1} and H_n then the fractional area and volume associated with it are

$$g_n = \int_{H_{n-1}}^{H_n} g dh, \qquad v_n = \int_{H_{n-1}}^{H_n} hg dh. \tag{2.2.2}$$

The average thickness over the distribution used in the momentum equation can then be calculated as

$$\bar{h} = \int_{H_0}^{H_{max}} hg dh = \sum_{n=1}^{N_{bins}} v_n. \tag{2.2.3}$$

An important component of the redistribution function, ψ, is the distribution of ice that participates in ridging (a_n). This is the function that determines what fraction of thinner ice

will compress to form a ridge. The distribution of ice that participates in ridging presented in Lipscomb *et al.* [21] is used for this analysis due to its improved stability over the original Thorndike *et al.* [37] function. The discrete form of the participating ice distribution after dividing into thickness bins is given by

$$a_n = \frac{\exp(-G_{n-1}/a^*) - \exp(-G_n/a^*)}{1 - \exp(-1/a^*)}. \tag{2.2.4}$$

Here $G_n = \sum_{m=0}^{n} a_m$ is the discrete cumulative distribution function and a^* is a fixed parameter, which has been selected as a parameter in the sensitivity analysis.

The other component of the redistribution function is the distribution of ice that has undergone ridging. The ridged ice distribution used for this analysis is also in the form of an exponential. Given an average thickness in each bin defined as $h_n = v_n/a_n$ then the distribution of ridged ice is proportional to

$$\exp\left(\frac{-(h - 2h_n)}{\mu(h_n)^{1/2}}\right), \tag{2.2.5}$$

where μ is another parameter varied in the sensitivity analysis.

2.3 Thermodynamics

Growth and melt of ice is incorporated in the governing equations through a one-dimensional heat equation that is solved to obtain the temperature distribution in a vertical column of ice as shown here [23, 2]

$$\rho c \frac{\partial T}{\partial t} = \frac{\partial}{\partial z}\left(k \frac{\partial T}{\partial z}\right) + \kappa i_0 F_{SW} \mathrm{e}^{-\kappa z}. \tag{2.3.1}$$

The internal heat source ($\kappa i_0 F_{SW} \mathrm{e}^{-\kappa z}$) in the equation depends on the extinction coefficient (κ), the fraction of solar radiation absorbed by the ice (i_0), and the total downward shortwave (solar) flux (F_{SW}). The heat capacity (c), and conductivity (k) are functions of temperature and salinity, where the salinity is described by a fixed profile depending on the vertical coordinate (z) as shown in Equation 2.3.2 where $a = 0.407$, $b = 0.573$, and $S_{max} = 3.2$ ppt.

$$S(z) = \frac{1}{2} S_{max}\left(1 - \cos(\pi z^{\frac{a}{z+b}}\right). \tag{2.3.2}$$

Given this salinity profile, the heat capacity and conductivity are calculated as

$$c(S,T) = c_0 + \frac{\mu_{melt} L_0 S(z)}{T^2} \tag{2.3.3}$$

$$k(S,T) = k_0 + \frac{\beta S(z)}{T}. \tag{2.3.4}$$

Here c_0, k_0, and L_0 are the fresh ice values for heat capacity, conductivity and latent heat, respectively, and μ_{melt} and β are fixed parameters. Based on their importance in a previous sensitivity study [16], S_{max} and k_0 were chosen as parameters in this analysis.

To obtain the change in thickness of the ice due to thermodynamic forcing the following balance of flux equations must be solved at the atmosphere and ocean interfaces

$$\begin{aligned} F_w - k\frac{\partial T}{\partial z} &= -q\frac{dh}{dt} \\ F_a + k\frac{\partial T}{\partial z} &= -q\frac{dh}{dt} \end{aligned} \tag{2.3.5}$$

where the enthalpy (q) is also dependent on the temperature and salinity. Note that dh/dt from both the ocean and atmosphere boundary in Equation (2.3.5) are combined to obtain the rate of change in thickness (f) in the ice thickness distribution equation (2.2.1).

The flux at the ocean interface (F_w) is simply the heat flux from the ocean to the ice calculated as a function of the ocean surface temperature and salinity. The net flux at the atmosphere interface (F_a) is a combination of flux terms as shown in Equation (2.3.6).

$$F_a = F_{SW} - F_{SW\uparrow} - F_{SW,trans} + F_{LW} - \epsilon\sigma T_0^4 + F_{sh} + F_{lh} \tag{2.3.6}$$

It includes the total shortwave flux due to solar radiation (F_{SW}) minus the fraction which is reflected based on the albedo of the surface ($F_{SW\uparrow}$) and the fraction that is transmitted through the ice $F_{SW,trans}$. It additionally includes the downward longwave flux due to atmospheric heating (F_{LW}) and the upward longwave flux from the ice surface ($\epsilon\sigma T_0^4$), which is defined in terms of the surface temperature (T_0), the Stefan-Boltzmann constant (σ) and the longwave emissivity of the surface (ϵ). The final terms in the balance are the flux of sensible heat (F_{sh}) and the flux of latent heat (F_{lh}), which are derived on the basis of atmospheric forcing input.

An important component of the thermodynamics is the proportion of shortwave flux that is reflected, which is dependent on the albedo (α), or reflectivity, of the ice or snow surface. In both codes an albedo parameterization that is temperature and thickness dependent is used [14]. The parameterization depends on inputs of the visual ice albedo ($\alpha_{ice,v}$), the near-infrared ice albedo ($\alpha_{ice,i}$), the visual snow albedo ($\alpha_{snow,v}$), and the near-infrared snow albedo ($\alpha_{snow,i}$). The ice albedo is first modified based on the thickness (h) of the column to produce a smooth decrease in ice albedo to the value of the ocean albedo (α_{ocean}) as the thickness decreases. The following functional form is used

$$\begin{aligned} \alpha_{ice,v} &= \alpha_{ice,v} f_h + \alpha_{ocean}\,(1 - f_h) \\ \alpha_{ice,i} &= \alpha_{ice,i} f_h + \alpha_{ocean}\,(1 - f_h) \end{aligned} \tag{2.3.7}$$

where the fractional thickness is defined using a maximum thickness for constant albedo of $h_{max} = 0.5$ as

$$f_h = \frac{\tan^{-1}(4h)}{\tan^{-1}(4h_{max})}. \tag{2.3.8}$$

The temperature dependence modification of the albedos is then applied based on the surface temperature (T_0) in the following manner

$$\begin{aligned} \alpha_{ice,v} &= \alpha_{ice,v} - 0.075(T_0 + 1) \\ \alpha_{ice,i} &= \alpha_{ice,i} - 0.075(T_0 + 1) \\ \alpha_{snow,v} &= \alpha_{snow,v} - 0.1(T_0 + 1) \\ \alpha_{snow,i} &= \alpha_{snow,i} - 0.15(T_0 + 1). \end{aligned} \tag{2.3.9}$$

The total albedo is calculated from the snow and ice albedos, which are combined based on the snow thickness (h_{snow}) and the snow fraction, $f_{snow} = h_{snow}/(h_{snow} + 0.02)$ as

$$\begin{aligned} \alpha_v &= \alpha_{ice,v}(1 - f_{snow}) + \alpha_{snow,v} f_{snow} \\ \alpha_i &= \alpha_{ice,i}(1 - f_{snow}) + \alpha_{snow,i} f_{snow}. \end{aligned} \tag{2.3.10}$$

Given the total shortwave radiation on the snow or ice surface, (F_{SW}), and the fractions of shortwave radation in the visual (f_v) and near-infrared range (f_i) the surface reflected, transmitted, and absorbed portions can then be calculated as

$$\begin{aligned} F_{SW\uparrow} &= F_{SW} f_i \alpha_i + F_{SW} f_v \alpha_v \\ F_{SW,trans} &= (F_{SW} - F_{SW\uparrow})(1 - f_{snow}) i_0 \\ F_{SW,abs} &= F_{SW} - F_{SW\uparrow} - F_{SW,trans}. \end{aligned} \tag{2.3.11}$$

For the sensitivity calculations the fraction of shortwave radiation that is transmitted through the ice (i_0) is evaluated along with the visual and near-infrared ice albedos ($\alpha_{ice,v}, \alpha_{ice,i}$) and the visual snow albedo ($\alpha_{snow,v}$).

Chapter 3

Simulations

3.1 Model Configurations

To evaluate the sensitivity of the two models to selected parameters, one year simulations of the Arctic basin were used. As discussed in the previous sections, the MPM sea ice code and the CICE model differ in both the rheology used to calculate stress and in the horizontal discretizations for the solution of the momentum equation and for advection of the ice thickness distribution. For the horizontal discretization CICE uses a staggered Eulerian grid (the Arakawa B-grid), which locates the ice area, volume, and energy at the cell centers and the ice velocity at the cell vertices [14]. Advection is modeled with a linear remapping scheme, which uses a limiter to preserve monotonicity [20].

The MPM sea ice model is based on the material-point method, which combines Lagrangian particles to handle advection of the ice properties, and a background grid where the momentum equation is solved and where gradients may be calculated easily [35, 36, 33]. At each time step particle information is mapped to a regular background grid where the momentum equation is solved using bilinear nodal finite elements. Quantities such as ice area, volume, and energy are transported in the velocity field with the particles and the constitutive model is solved at each material point. External forces are applied at the nodes of the background grid for the momentum equation solution.

The horizontal transport component of the ice thickness distribution equation is solved using the remapping scheme in the case of CICE and in a Lagrangian manner in the case of MPM. However, transport in thickness space is solved in the same way for both MPM and CICE using a linear remapping algorithm due to Lipscomb [19]. Also, the same ridging function is used for both codes. The ice thickness distribution is divided into five fixed categories of ice and one category for open water in both CICE and MPM and the same uniform thickness distribution was used for initial conditions. The distribution is assumed to be parabolic with a maximum at $h = 3m$ and values of zero at $h = 0m$ and $h = 6m$ and is shown in Figure 3.1.1.

The energy conserving Bitz and Lipscomb [2] algorithm is used to solve the vertical temperature equation for the change in thickness due to thermodynamics in both the MPM sea ice code and the LANL CICE code. For the discretization, five layers of ice and one layer of snow were used.

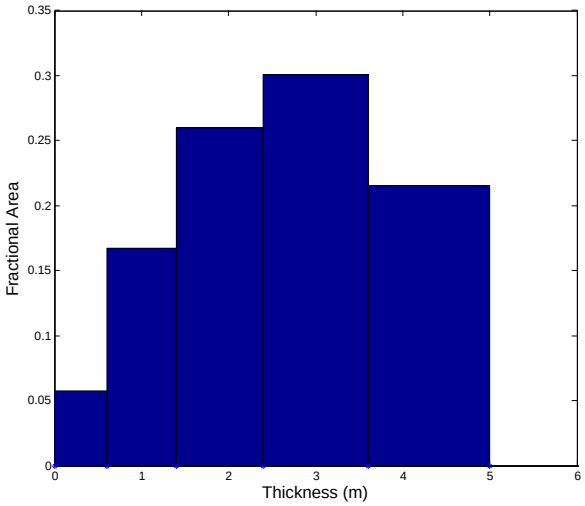

Figure 3.1.1: The ice thickness distribution used in both the MPM and CICE calculations for regions where ice is initially assumed to exist.

The initial configuration of the grid is shown in Figure 3.1.2. A grid with 148x124 square cells of length 50 km was used for CICE and for the background grid in MPM. Additionally, four material points per cell were used in the MPM calculation. In CICE, a cell land mask is used to determine which cells are active within the calculation. In the MPM sea ice code fixed particles are used to represent the land boundaries. This results in a slight difference in the definition of the land boundary, since the MPM calculation allows for cells with partial land fill. Although CICE is generally run in spherical coordinates, the simulations were done in Cartesian coordinates using an azimuthal equal area mapping. This was done to provide a direct comparison with the MPM sea ice code, which is currently limited to a Cartesian grid.

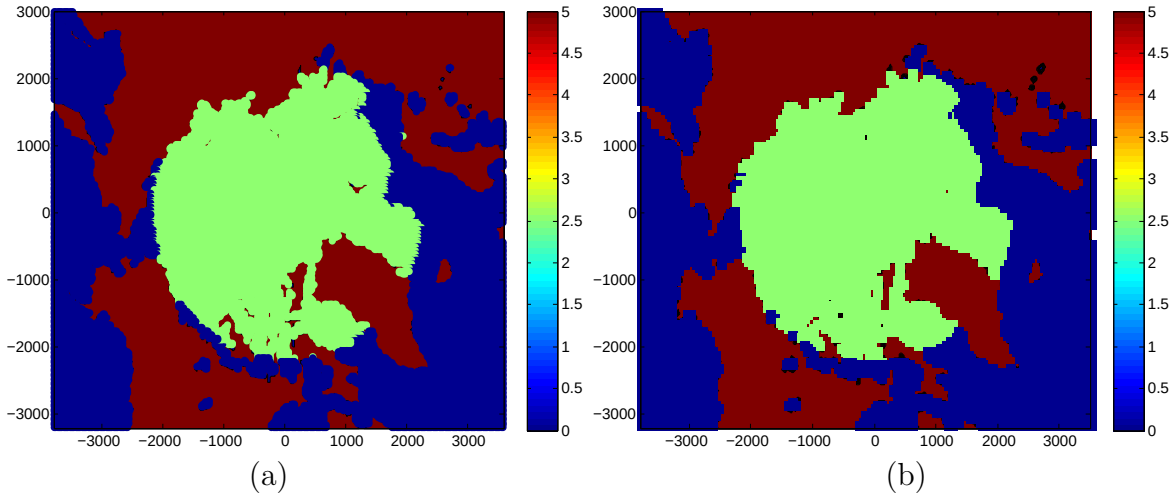

Figure 3.1.2: The computational domain for the pan-Arctic calculation (land regions in red) showing initial average thickness for (a) the MPM calculation and (b) the CICE calculation.

3.2 External Forcing

Both ice models are run in stand alone mode and therefore ocean and atmospheric forcing are required to drive the simulations. The ocean forcing data comes from the Pan-Arctic Ice-Ocean Modeling and Assimilation System (PIOMAS) data sets [38], and consists of monthly spatially varying sea surface salinity (SSS), sea surface temperature (SST), and ocean currents. The SSS is used to calculate a freezing temperature for the ocean water, which is used with the SST to calculate the ocean flux. In the case of CICE, a simple ocean mixed layer is used where the ocean temperature and salinity may change during a run due to radiative fluxes that pass through the ice and fresh water or salt fluxes ejected from the ice as it melts or freezes. Although CICE modifies the SST, the code is set up to restore the calculated SST values to the data over the period of thirty days. However, the MPM sea ice calculation simply uses the prescribed SST and SSS fields.

Atmospheric data from the Common Ocean-ice Reference Experiments (CORE) version 2 [18], which contain high latitude corrections to the National Center for Atmospheric Research (NCAR) / National Center for Environmental Protection (NCEP) reanalysis data [15], are used to drive the simulations. The data include spatially varying six-hourly atmospheric winds, specific humidity, and air temperature as well as daily spatially varying downward shortwave (solar) flux and monthly precipitation. Monthly spatially varying cloud fractions are taken from the Ocean Model Intercomparison Project (OMIP) data [27]. The downward longwave flux from the atmosphere is then derived from the air temperature (T_a) and cloud fraction (c_{frac}) using the Parkinson and Washington formula [26].

In all cases linear interpolation in time is used to derive the forcing for a given time step in both the MPM and CICE codes.

3.3 Results for Nominal Simulation

At the start of the simulations the ice is assumed to be at rest with a surface temperature equal to the air temperature and an initial energy that corresponds to the linear temperature profile through the ice. The simulation is run for a single year. A timestep of two hours is used in the CICE calculations with 120 subcycles for the dynamics. For the MPM calculations the timestep is limited to a maximum of 500 seconds due to dynamic instabilities that develop at the ice-ocean edge along the East coast of Greenland when higher values are used.

The spatial distribution of ice thickness at the end of September (close to the ice extent minimum) and at the end of December (the final time for the calculation) for the standard simulation is shown in Figure 3.3.1. The ice thickness plots show considerable variation between the codes, in particular the December ice thickness plot for the MPM code has considerably more thick ice ($\sim$ 3 meters) than the CICE code. This may be due in part to the different rheologies implemented in the code. The ice is assumed to be intact in the initial conditions, making it stiffer and less likely to deform significantly over the year.

This difference may be also due in part to small differences in the implementation of the thermodynamics. An additional difference is the prominence of the thick ice boundary in the MPM results compared to the CICE results. This is due primarily to the fact that the ice thickness distribution is associated with a Lagrangian point in the MPM code and therefore there is less diffusion in the ice thickness from the advection scheme.

Similarly, the ice velocity comparison (Figure 3.3.2) also indicates some discrepancy between the codes. This, however, is expected because the rheologies are considerably different. The ice velocity in the central Arctic tends to be smaller in the MPM simulation consistent with an ice pack having greater strength. However, both codes predict large velocities off the Eastern coast of Greenland and have circulation patterns consistent with a gyre in the Beaufort Sea region.

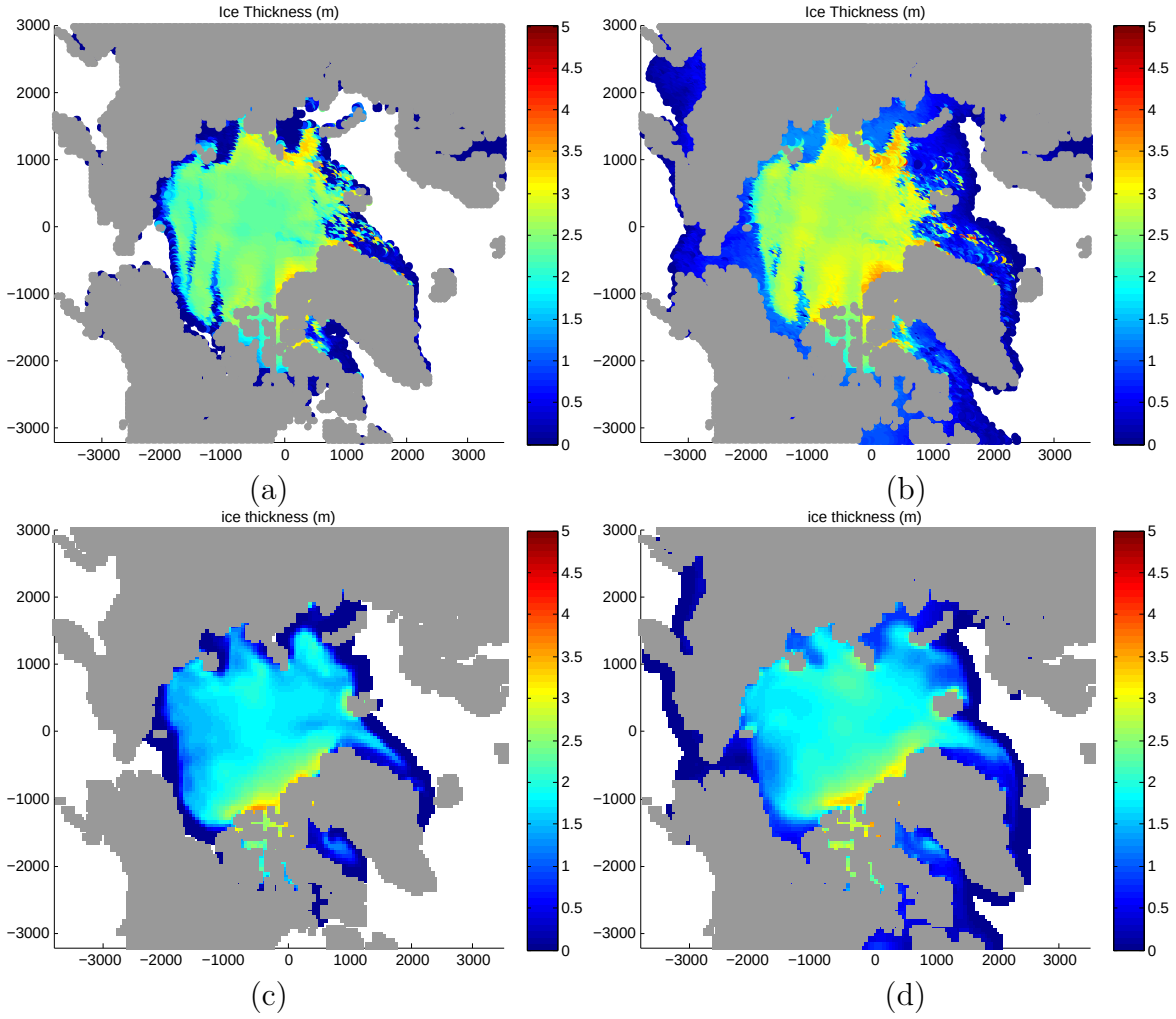

Figure 3.3.1: The ice thickness in meters for (a) the MPM calculation at the end of September, (b) the MPM calculation at the end of December, (c) the CICE calculation at the end of September, (d) the CICE calculation at the end of December.

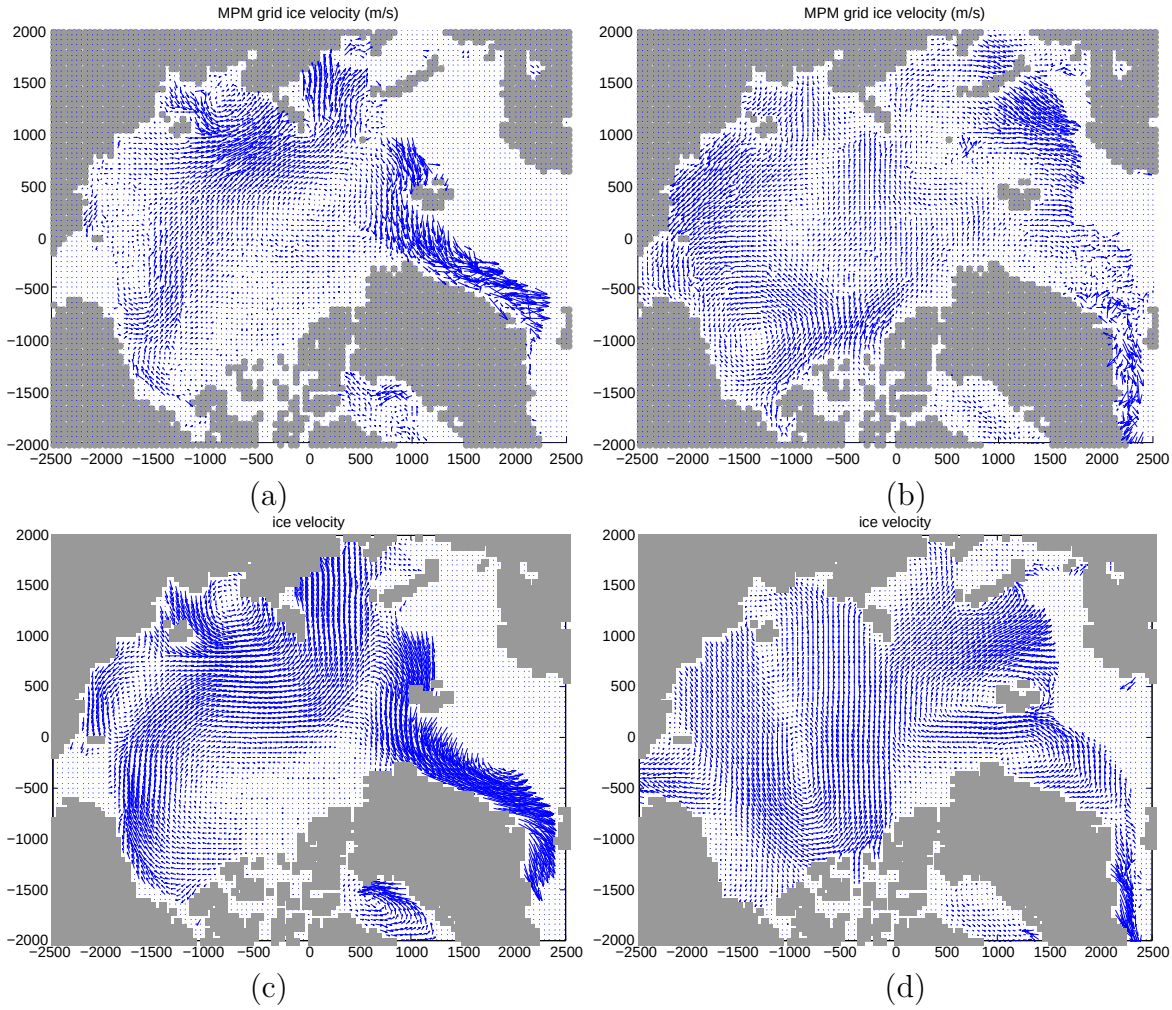

Figure 3.3.2: The ice velocity for (a) the MPM calculation at the end of September, (b) the MPM calculation at the end of December, (c) the CICE calculation at the end of September, (d) the CICE calculation at the end of December.

Chapter 4

Sensitivity Analysis

4.1 Parameter Selection

Parameters of interest for the sensitivity analysis were chosen based on their impact in previous sensitivity studies and their common inclusion in both the CICE and MPM sea ice models [16, 14]. They can be broadly classified as either dynamic or thermodynamic parameters depending on whether they primarily influence ice deformation or ice growth and melt. The model parameters evaluated in the sensitivity analysis are shown in Table

Table 4.1.1: Model Parameters for Sensitivity Analysis.

Parameter	Nominal Value	Range	Description
$\alpha_{ice,v}$	0.78	0.7-0.86	Visual ice albedo
$\alpha_{ice,i}$	0.36	0.32-0.4	Near-infrared ice albedo
$\alpha_{snow,v}$	0.98	0.88-1.0	Visual snow albedo
ϵ	0.95	0.85-1.0	Emissivity
i_0	0.70	0.63-0.77	Fraction of shortwave radiation penetrating ice
k_0	2.03	1.827-2.233	Fresh ice conductivity $(W/(mK))$
S_{max}	3.2	2.88-3.52	Maximum salinity (ppt)
c_w	0.0055	.00495-.00605	Ice-ocean drag parameter
a^*	0.05	0.045-0.055	Ridging parameter
μ	4	3.6-4.4	Ridging parameter

4.1.1 with their given nominal values and the sampling ranges used in the sensitivity analysis. The ranges are centered around the nominal value and the upper and lower bounds of the ranges are represented by $+/-10\%$ spread around the nominal values, except in the cases of the emissivity and visual snow albedo where the upper limit cannot go beyond one.

The dynamic parameters for consideration in the study are limited given that the MPM and CICE models use different rheologies. Additionally, the treatment of atmospheric dynamic forcing is different in each code. Therefore, the dynamic parameters were chosen from the ocean dynamic forcing and ridging algorithms. These include the ice-ocean drag

coefficient (c_w) and two ridging parameters (a^*, μ). Among the set of possible thermodynamic parameters, albedo is known to have a strong effect on ice seasonal growth and melt. Therefore, three albedo parameters were used in this analysis, the visual ice albedo ($\alpha_{ice,v}$), near-infrared ice albedo ($\alpha_{ice,i}$), and visual snow albedo ($\alpha_{snow,v}$). Like the albedo, the fraction of shortwave radiation that penetrates the ice (i_0) and the longwave emissivity of the surface (ϵ) can also have an important effect on the growth and melt of ice. The study of Kim *et al.* [16] found that the fresh ice conductivity (k_0) and maximum salinity (S_{max}) were important parameters and were used in this analysis to complete the set of thermodynamic parameters.

Table 4.1.2: Response Functions for Sensitivity Analysis.

Variable	Description
A_{tot}	Total ice area (km^2)
E_{tot}	Total ice extent (km^2)
V_{tot}	Total ice volume (m^3)
$\mathbf{v}_{rms}$	RMS ice speed (m/s)
h_{CA}	Central Arctic ice thickness (m)
$\mathbf{v}_{CA}$	Central Arctic ice speed(m/s)

The response functions were chosen because of their importance in assessing the state of the Arctic ice pack and are listed in Table 4.1.2. Total ice area (A_{tot}) and total ice extent (E_{tot}) are related quantities and are calculated using the ice concentration or fractional area of ice either in a cell or associated with a material point. In the case of ice area, the partial area of a cell or material point that is ice covered is summed over the calculational domain. In contrast, for the ice extent, the total areas of cells or material points that contain at least fifteen percent ice are summed. Therefore, in the winter when the ice concentration is high the ice area and ice extent match closely, but in the summer the values diverge as more open water is exposed reducing the ice concentration. Both ice area and ice extent are quantities diagnosed from satellite data and are therefore of importance for comparing with actual Arctic data.

The total ice volume (V_{tot}) is arguably a more important indicator of the health of the Arctic ice, which is why it was chosen as a response function here, but it is difficult to measure remotely and there is not a significant amount of data for comparison. The root mean square (RMS) speed of the ice (v_{rms}) is strongly dependent on the ocean and atmospheric dynamic forcing of the ice as well as the strength of the ice and was chosen as a response function because ice velocity is one of the primary unknowns in the governing equations. In addition to these four global response functions, ice thickness (h_{CA}) and speed ($\mathbf{v}_{CA}$) at the North Pole were chosen to assess the variability of local values.

4.2 Methodology

In this section we provide a necessarily brief summary of the methodology used to carry out the sensitivity analysis (SA) studies and its specialization to the sea-ice models considered in this report. Our presentation closely follows the approach outlined in [8].

4.2.1 Background

The definition in [28] states that SA studies the relationships between the information flowing in and out of the model. Originally, SA was created to deal simply with uncertainties in the input variables and model parameters. Over the time, the idea has been extended to incorporate the conceptual uncertainties associated with the model such as uncertainties in the model structure, assumptions and specifications. In general, SA is used to increase the confidence in the model structure and in the model predictions, by providing understanding of how the model outputs respond to changes in the inputs, model structure, or factors such as models independent components [28]. SA is therefore closely connected to uncertainty analysis which aims to quantify the overall uncertainty associated with the response as a result of uncertainty in the model's inputs.

SA is usually performed to determine [28]:

- whether a model resembles the system or process under study;
- the model's parameters that contribute most significantly to the output variability and that require additional research and understanding;
- the model parameters that are insignificant and that can be potentially eliminated from the final model;
- the region(s) in parameter space where the model variation is the greatest;
- the optimal regions in the parameters space that can be used for model calibration;
- interaction between parameters;

Sampling-based SA is a type of study in which the computational model is executed multiple times for a combination of parameter values sampled from distributions. Monte Carlo analysis is an example of sampling-based SA, based on performing multiple solution evaluations with randomly selected model inputs. Monte Carlo analysis next uses the results of these evaluations to determine both uncertainty in the model prediction and which parameters mainly contribute to this uncertainty. In general, Monte Carlo analysis involves five distinct steps [28, 8]: (1) selection of ranges and distributions for each parameter; (2) generation of samples from the ranges of the distributions; (3) evaluation of the model for each sample followed by (4) uncertainty and (5) sensitivity analysis.

Various sampling procedures can be used for Monte Carlo studies among which are random sampling, quasi-random sampling and stratified sampling including Latin Hypercube Sampling (LHS) [28, 8]. In LHS the range of each input parameter is divided into N equally likely intervals and one observation of each input parameter is made in each interval. Thus, there are N non-overlapping realizations for each of the k input parameters. The method has the advantage of ensuring that the input parameter has all portions of its input distribution represented by its input values. The LHS performs better compared to random and quasi-random sampling when the output is dominated by only few components of the input parameters. The method ensures that each of these components is represented in a fully stratified manner, no matter which component turns out to be important. Stein [31] proved that, asymptotically, LHS is better than random sampling in that it provides an estimator with lower variance. In particular, he showed that the closer the output function is to being additive with respect to input variables, the greater is the reduction in the variance. Nevertheless, there are still examples in which for non-additive and monotonic functions, the performance of LHS is equivalent or worse than the performance of simple random sampling.

For this sensitivity and uncertainty propagation study we implemented Monte Carlo analysis based on LHS.

4.2.2 Linear regression model

Sensitivity analysis performed as part of Monte Carlo studies is often based on linear regression model. This approach assumes linear relationship between inputs and outputs given by

$$y = a_o + \sum_{j=1}^{n} a_j x_j, \tag{4.2.1}$$

where y is the response (output), x_j are the input variables (parameters) under consideration, and a_j are coefficients that must be determined. The coefficients a_j and other aspects of the construction of the regression model shown in (4.2.1) can be used to assess the importance of the individual input variables x_j with respect to the observed uncertainty in the output (response function) y.

The construction of the regression model in (4.2.1) is as follows. Suppose that we are given a sequence y_i, $i = 1, \ldots, m$ of output values, each corresponding to a set x_{ij}, $j = 1, \ldots, n$ of input parameters. Assuming that the linear model (4.2.1) is valid (holds) for each response value we can write

$$y_i = a_o + \sum_{j=1}^{n} a_j x_{ij} + \varepsilon_i. \tag{4.2.2}$$

Typically, in a Monte Carlo study the number of responses m is much greater than the number of input parameters n, thereby making (4.2.2) an overdetermined $m \times n$ algebraic system for the unknown coefficients a_j. The method of least squares is widely used to solve such systems and will be employed here. To determine the a_j, it is convenient to use the

following matrix representation for the equations in (4.2.2)

$$\mathbf{y} = \mathbf{X}\mathbf{a} + \boldsymbol{\varepsilon}, \tag{4.2.3}$$

where $\mathbf{y} = (y_1, \ldots, y_m)^T$, $\mathbf{a} = (a_0, \ldots, a_n)^T$, $\boldsymbol{\varepsilon} = (\varepsilon_1, \ldots, \varepsilon_n)^T$ and $\mathbf{X}$ is m by $n+1$ array of the input variables augmented with column of all ones.

In the least squares approach, the coefficients a_j are determined by minimizing the quadratic functional formed by summing up the squares of the residuals of the equations in the overdetermined system. Succinctly, this functional can be written as

$$R(\mathbf{a}) = \sum_{i=1}^{m}(y_i - a_0 - \sum_{j=1}^{n} a_j x_{ij})^2 = (\mathbf{y} - \mathbf{X}\mathbf{a})^T(\mathbf{y} - \mathbf{X}\mathbf{a})\,. \tag{4.2.4}$$

A necessary condition for minimizers of (4.2.4) is obtained by setting the gradient of the least-squares functional $R(\mathbf{a})$ to zero. This yields the following $(n+1) \times (n+1)$ linear system for the unknowns a_j

$$\mathbf{X}^T\mathbf{X}\mathbf{a} = \mathbf{X}^T\mathbf{y}\,. \tag{4.2.5}$$

The linear system (4.2.5) is known as the *normal equations*. If $\mathbf{X}$ has full column rank, i.e., its columns are linearly independent, it is easy to see that $\mathbf{X}^T\mathbf{X}$ is invertible. The unique solution $\mathbf{a}$ of the normal equations is then given by the formula

$$\mathbf{a} = \left(\mathbf{X}^T\mathbf{X}\right)^{-1}\mathbf{X}^T\mathbf{y}\,. \tag{4.2.6}$$

As a rule, when the overdetermined system is obtained through a Monte Carlo study, $\mathbf{X}$ does have full column rank and the normal equations have a unique solution.

The following identity holds [28, 8] for the least squares regression model and plays an important role in assessing the adequacy of such models

$$\sum_i (y_i - \bar{y})^2 = \sum_i (\hat{y}_i - \bar{y})^2 + \sum_i (\hat{y}_i - y_i)^2, \tag{4.2.7}$$

where $\hat{y}_i$ denotes the estimate of y_i obtained from the regression model and $\bar{y}$ is the mean of y_i. Since the quantity

$$\sum_i (\hat{y}_i - \bar{y})$$

provides a measure of variability about the regression line, the ratio

$$R^2 = \frac{\sum_i (\hat{y}_i - \bar{y})^2}{\sum_i (y_i - \bar{y})^2}$$

provides a measure of the extent to which the regression model can match the observed data. Specifically, when the variation about the regression line $\sum_i (\hat{y}_i - y_i)^2$ is small relative to $\sum_i (\hat{y}_i - \bar{y})^2$, then the corresponding R^2 value is close to 1, which indicates that the regression model is accounting for most of the variability in the y_i. Conversely, an R^2 value

close to zero indicates that the regression model is not very successful in accounting for the variability in the y_i.

The regression model in (4.2.1) can be algebraically reformulated as

$$(y - \bar{y})/\hat{s} = \sum_j \frac{(a_j \hat{s}_j/\hat{s})(x_j - \bar{x}_j)}{\hat{s}_j}, \tag{4.2.8}$$

where

$$\bar{y} = \sum_i \frac{y_i}{m}, \hat{s} = \Big(\sum_i \frac{(y_i - \bar{y})^2}{(m-1)}\Big)^{1/2}, \tag{4.2.9}$$

and

$$\bar{x}_j = \sum_i \frac{x_{ij}}{m}, \hat{s} = \Big(\sum_i \frac{(x_{ij} - \bar{x}_j)^2}{(m-1)}\Big)^{1/2}. \tag{4.2.10}$$

The coefficients $a_j \hat{s}_j/\hat{s}$ in (4.2.8) are called standardized regression coefficients. Their values are scaled in the range of -1 to 1. When the x_j are independent, the absolute value of the standardized regression coefficients can be used to provide a measure of variable importance with respect to observed uncertainty in the response function. Specifically, the coefficients provide a measure of importance based on the effect of moving each variable away from its expected value by a fixed fraction of its standard deviation while retaining all other variables at their expected values [28, 8]. Calculating standardized regression coefficients is equivalent to performing the regression analysis with the input and output variables normalized to mean zero and standard deviation one. The sign of the standardized regression coefficients indicates the direction of change of the response function with respect to the direction of change in the input. The "-" sign indicates that increase in the value of the input parameter leads to decrease in the observed response function and vice-versa. Conversely, the "+" sign indicates that an increase in the value of the input leads to an increase in the value of the observed response function and a decrease in the value of the input leads to a decrease in the value of the observed response function.

4.2.3 Application to sea-ice models

We consider two kinds of sensitivity analysis studies for the CICE and MPM models. In the first one, we hold all but one of the ten input parameters in Table 4.1.1 fixed at their nominal values given in that table. This type of study is also known as one-at-a-time (OAT) screening designs and is intended to examine sensitivity of the six response functions in Table 4.1.2 viewed as functions of a single input parameter. One limitation of OAT design is that it does not enable estimation of interactions among inputs [28, 8].

In the second study we allow all input parameters to vary simultaneously in the ranges specified in Table 4.1.1. The purpose of this study is to consider the sensitivity of the six monitored outputs simultaneously with respect to all ten inputs. In other words, we assume that each response is a function of ten input parameters.

For both kinds of sensitivity analysis we assume the linear model (4.2.1) for each one of the six response functions (outputs) given in Table 4.1.2. Let ρ^k denote the k^{th} response function in Table 4.1.2. Application of (4.2.1) for the first sensitivity analysis scenario yields the linear model

$$\rho^k = a_0 + a_1^k x\,, \quad k = 1, \ldots, 6\,, \tag{4.2.11}$$

where x is the selected input parameter from Table 4.1.1. In the second case, application of (4.2.1) yields

$$\begin{aligned}\rho^k = a_0 + a_1^k \alpha_{ice,v} + a_2^k \alpha_{ice,v} + a_3^k \alpha_{snow,v} + a_4^k \epsilon \\ + a_5^k i_0 + a_6^k k_0 + a_7^k S_{max} + a_8^k c_w + a_9^k a^* + a_{10}^k \mu\end{aligned}\,, \quad k = 1, \ldots, 6\,, \tag{4.2.12}$$

The regression methodology described in the previous section is applied to each one of the response functions. For the OAT study we sample the response ρ^k at 6 uniformly spaced points in the range of the respective parameter x specified in Table 4.1.1. For the second type of study we use the LHS functionality of the DAKOTA toolkit [1] to generate sample sets

$$\{(\alpha_{ice,v})_i, (\alpha_{ice,v})_i, (\alpha_{snow,v})_i, (\epsilon)_i, (i_0)_i, (k_0)_i, (S_{max})_i, (c_w)_i, (a^*)_i, (\mu)_i\} \quad i = 1, \ldots, 50$$

where each parameter varies in the range specified in Table 4.1.1. Therefore, in the first study (4.2.2) corresponds to a 6×1 overdetermined linear system, whereas in the second study it is a 50×10 linear system.

We record the values of the response functions from CICE and MPM over a period of one year. The linear regression models (4.2.11) and (4.2.12) are then applied to the output values at or near the end of each month to compute the standardized regression coefficients as defined in (4.2.8). In doing so, we obtain a time series giving the standardized regression coefficients for CICE and MPM as functions of the calendar day. These series are compared to provide a measure of the equivalence of the responses by the two codes.

4.3 Single Parameter Sensitivity Results

For the single parameter sensitivity study (OAT) where each parameter was varied individually, a comparison can be made of the behavior of the response function with respect to a given parameter between the two sea ice codes. These results indicate whether a parameter is important to a given response function. However, these results do not provide information on how strong the response is compared with other parameters.

In Figure 4.3.1 the standardized regression coefficients for total ice area with respect to the ten parameters of interest are shown. The blue curve is the result from CICE and the red curve is the MPM result. CICE tends to exhibit simple, in many cases constant over the year, responses to the parameter variation. For example, the total ice area change with respect to all three albedo parameters ($\alpha_{ice,v}, \alpha_{ice,i}, \alpha_{snow,v}$), the emissivity ($\epsilon$), and the fresh ice conductivity (k_0) shows strong positive response and the total ice area change with

respect to maximum salinity (S_{max}) shows strong negative response. In each of these cases the MPM results are significantly noisier although MPM does show positive response for the middle part of the year for the albedos, the emissivity, and the fresh ice conductivity. Interestingly, the total ice area displays a similar response in both CICE and MPM for the ice-ocean drag coefficient (c_w), which is positive in April through October and negative for the rest of the year. The standardized regression coefficients for total ice extent (Figure 4.3.1) show similar behavior to the coefficients for total ice area, except for the case of the ridging parameter a^*, which indicates a positive response for the first seven months of the year. Although the responses are somewhat noisier we still see positive response for albedo ($\alpha_{ice,v}, \alpha_{ice,i}, \alpha_{snow,v}$), emissivity ($\epsilon$), and conductivity ($k_0$).

Figure 4.3.3 displays the standardized regression coefficients for total ice volume with respect to each of the ten parameters. For this response, the MPM and CICE coefficients show similar sensitivity and input-to-output correlations for most of the thermodynamic variables. The albedos ($\alpha_{ice,v}, \alpha_{ice,i}, \alpha_{snow,v}$), the emissivity ($\epsilon$), the fraction of shortwave radiation absorbed (i_0) and the fresh ice conductivity (k_0) all show a positive response for at least half of the year. Strangely, the maximum salinity (S_{max}), ridging parameter a^*, and ridging parameter μ exhibit strongly negative responses for CICE and mostly positive responses for MPM. This may result from an overall weak dependence of ice volume to these parameters, such that responses in either direction may be observed.

The standardized regression coefficients for RMS ice speed with respect to most of the parameters are noisy for MPM and exhibit quite a bit of variation for CICE (Figure 4.3.4). However, both codes display a strong negative response with respect to the ice-ocean drag coefficient (c_w). This is consistent with the physical mechanism of a larger drag reducing the velocity of the ice.

Results for the single parameter study evaluation of central Arctic ice thickness, shown in Figure 4.3.6, are quite similar to results for total ice volume. In this case both the MPM and CICE results display a strong positive sensitivity to the albedo parameters ($\alpha_{ice,v}, \alpha_{ice,i}, \alpha_{snow,v}$), the emissivity ($\epsilon$), the fraction of shortwave penetrating the ice (i_0), and fresh ice conductivity (k_0), in the second half of the year. Again the standardized regression coefficient responses for maximum salinity (S_{max}) and the ridging parameter a^* are nearly opposite for MPM and CICE.

As with the RMS ice speed results, the standardized regression coefficients for the central Arctic ice speed are quite noisy for all parameters except the ice-ocean drag coefficient (c_w), which exhibits strong negative response (Figure 4.3.6).

4.4 Multi-Parameter Sensitivity Results

More interesting and perhaps more significant results can be derived from the multi-parameter studies where a ranking of variable importance may be obtained. For the multi-parameter studies the standardized regression coefficients for the MPM and CICE runs show many

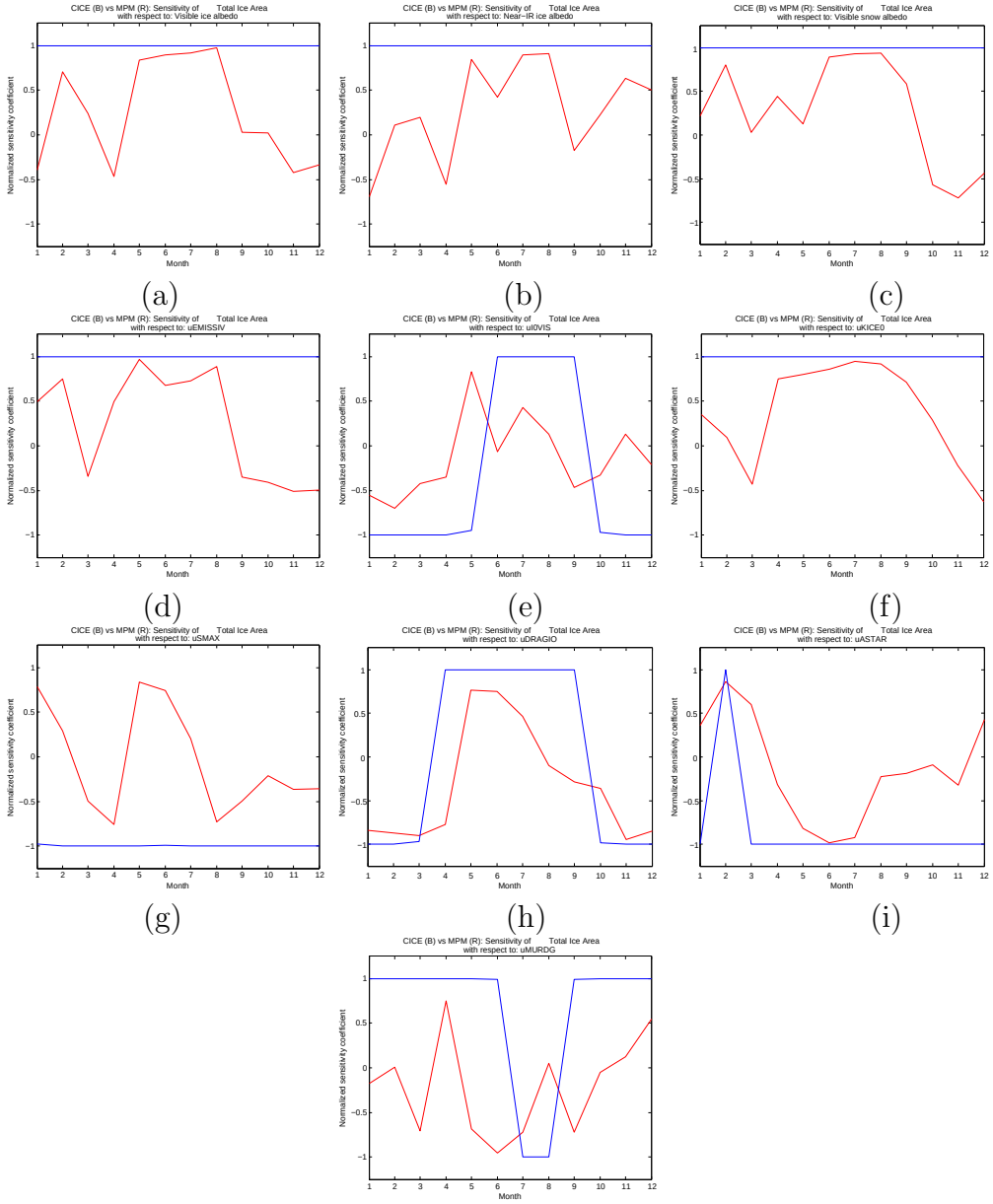

Figure 4.3.1: Normalized sensitivity of total ice area with respect to (a) visual ice albedo, (b) near-infrared ice albedo, (c) visual snow albedo, (d) emissivity, (e) fraction of shortwave absorbed by ice, (f) fresh ice conductivity, (g) maximum salinity, (h) ice-ocean drag coefficient, (i) ridging parameter a^*, and (j) ridging parameter μ. (MPM curve in red and CICE curve in blue.)

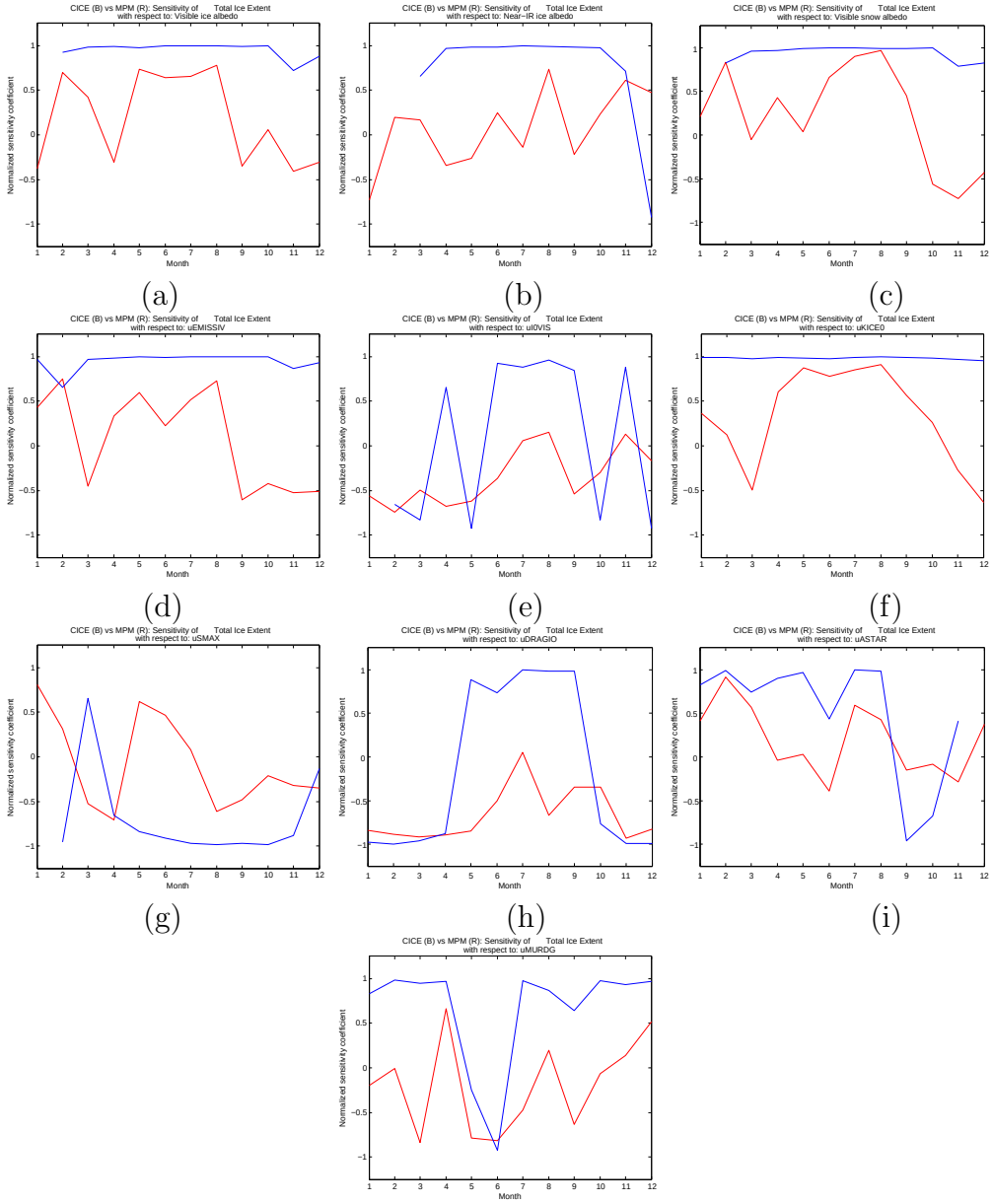

Figure 4.3.2: Standardized regresion coefficients for total ice extent with respect to (a) visual ice albedo, (b) near-infrared ice albedo, (c) visual snow albedo, (d) emissivity, (e) fraction of shortwave absorbed by ice, (f) fresh ice conductivity, (g) maximum salinity, (h) ice-ocean drag coefficient, (i) ridging parameter a^*, and (j) ridging parameter μ. (MPM curve in red and CICE curve in blue.)

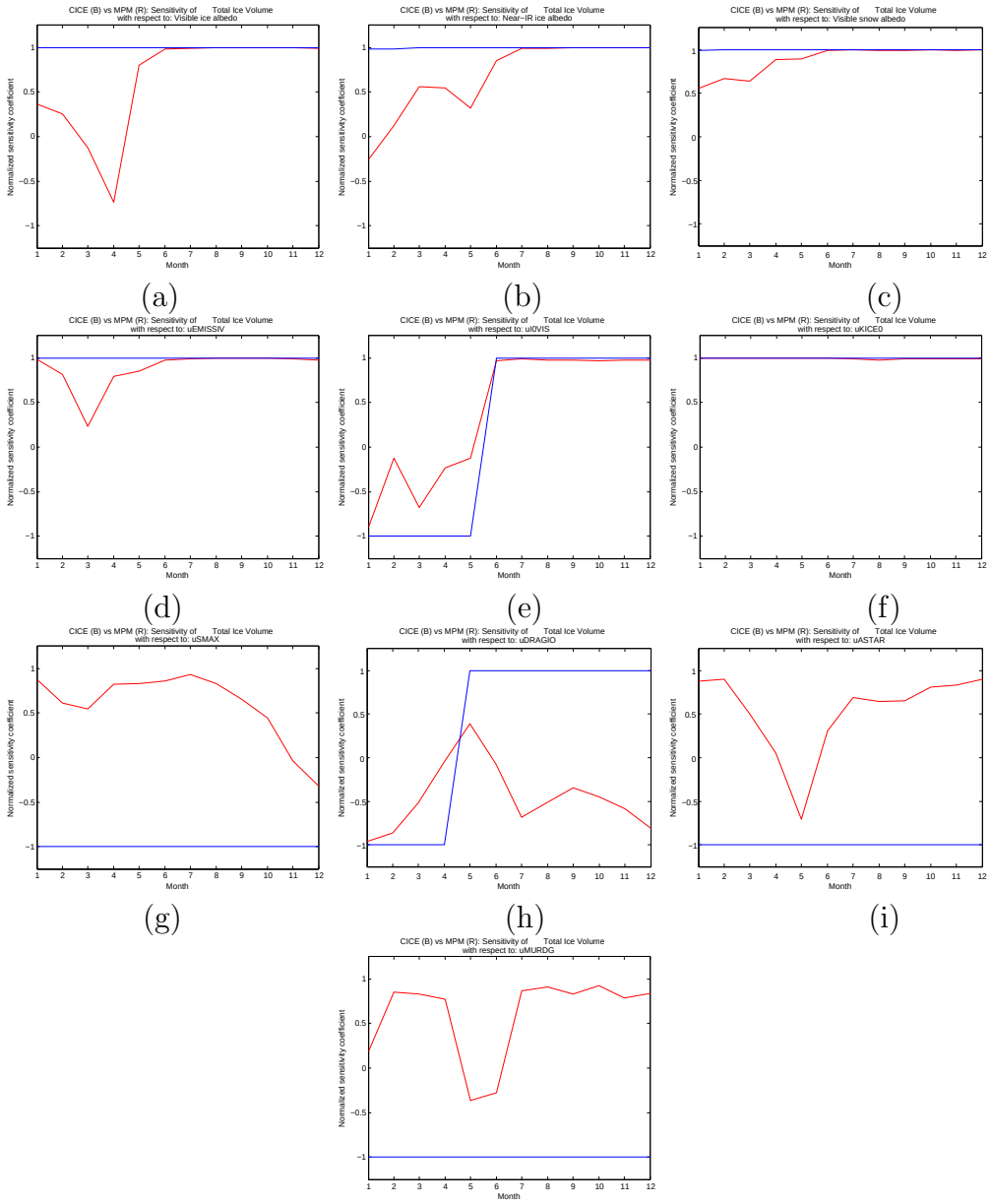

Figure 4.3.3: Standardized regression coefficients for total ice volume with respect to (a) visual ice albedo, (b) near-infrared ice albedo, (c) visual snow albedo, (d) emissivity, (e) fraction of shortwave absorbed by ice, (f) fresh ice conductivity, (g) maximum salinity, (h) ice-ocean drag coefficient, (i) ridging parameter a^*, and (j) ridging parameter μ. (MPM curve in red and CICE curve in blue.)

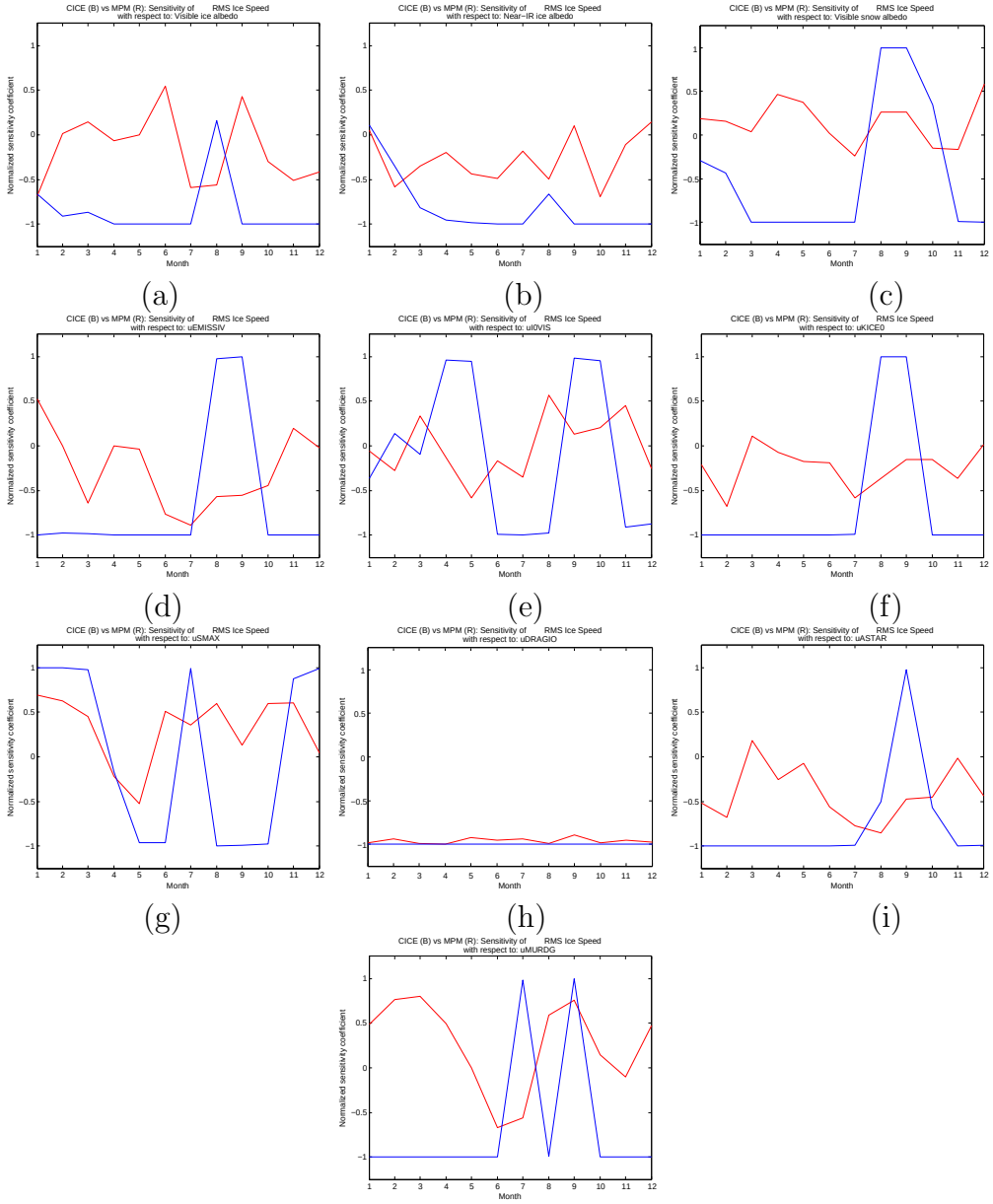

Figure 4.3.4: Standardized regression coefficients for RMS ice speed with respect to (a) visual ice albedo, (b) near-infrared ice albedo, (c) visual snow albedo, (d) emissivity, (e) fraction of shortwave absorbed by ice, (f) fresh ice conductivity, (g) maximum salinity, (h) ice-ocean drag coefficient, (i) ridging parameter a^*, and (j) ridging parameter μ. (MPM curve in red and CICE curve in blue.)

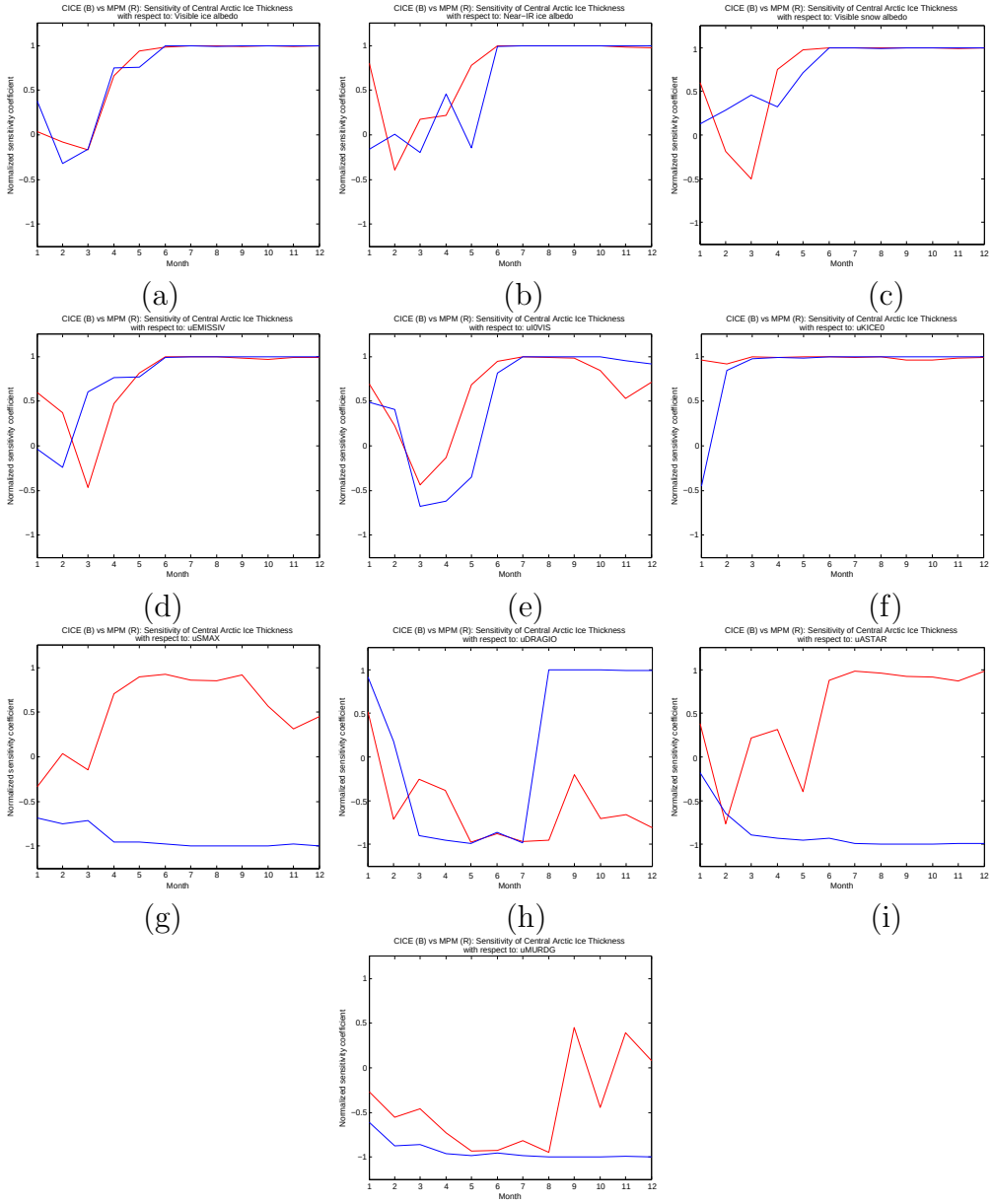

Figure 4.3.5: Standardized regression coefficients for central Arctic ice thickness with respect to (a) visual ice albedo, (b) near-infrared ice albedo, (c) visual snow albedo, (d) emissivity, (e) fraction of shortwave absorbed by ice, (f) fresh ice conductivity, (g) maximum salinity, (h) ice-ocean drag coefficient, (i) ridging parameter a^*, and (j) ridging parameter μ. (MPM curve in red and CICE curve in blue.)

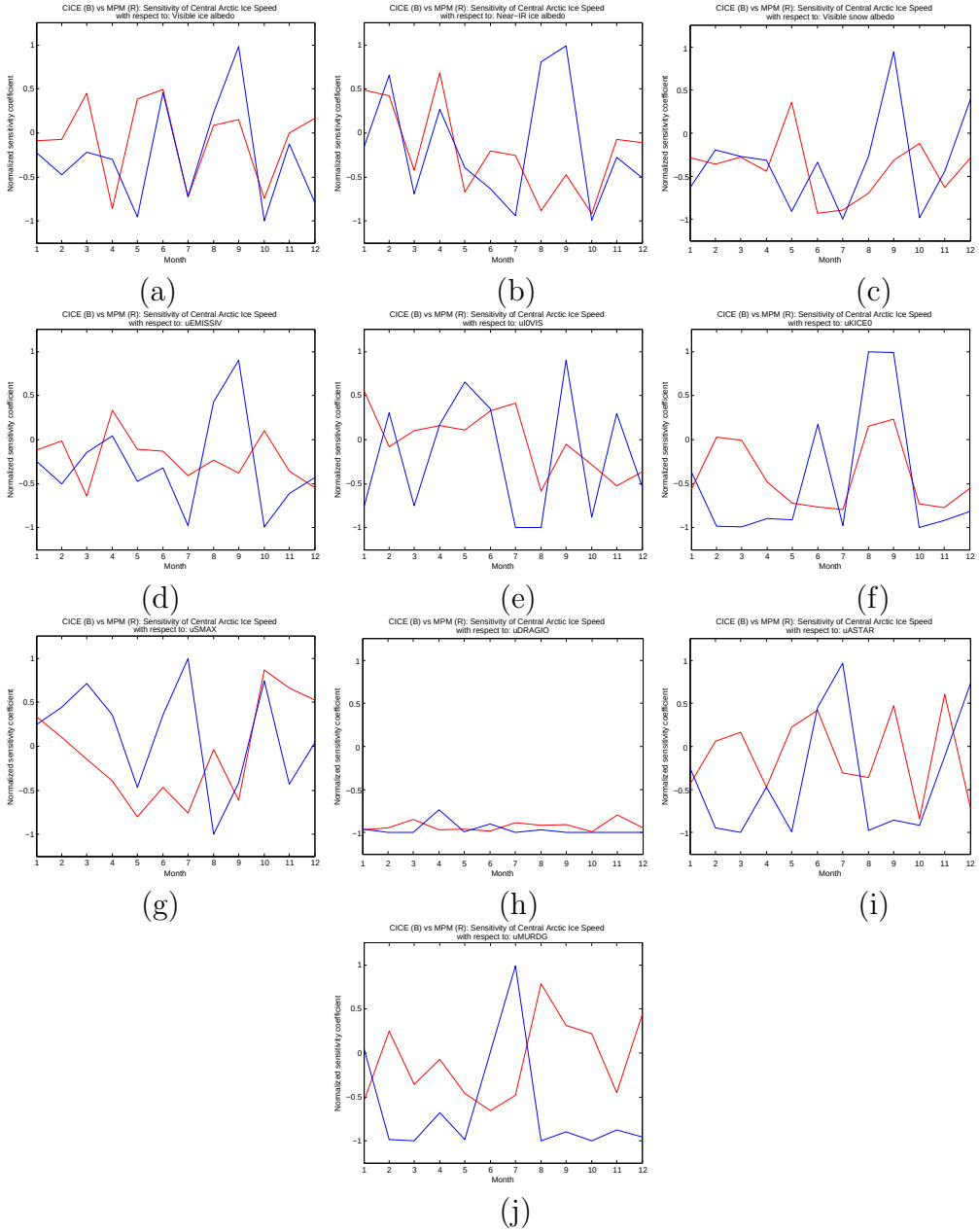

Figure 4.3.6: Standardized regression coefficients for central Arctic ice speed with respect to (a) visual ice albedo, (b) near-infrared ice albedo, (c) visual snow albedo, (d) emissivity, (e) fraction of shortwave absorbed by ice, (f) fresh ice conductivity, (g) maximum salinity, (h) ice-ocean drag coefficient, (i) ridging parameter a^*, and (j) ridging parameter μ. (MPM curve in red and CICE curve in blue.)

similarities as seen in Figures 4.4.1 - 4.4.6.

As with the single-parameter results, the total ice area and total ice extent show similar sensitivity responses (Figure 4.4.1, Figure 4.4.2). For both CICE and MPM, the total ice area and extent display strong negative sensitivity responses to the ocean drag coefficient (c_w) at the beginning and end of the year corresponding to times where there is a considerable amount of new thin ice. This is a plausible response since a higher drag coefficient will reduce the velocity of the ice and thereby reduce the amount of thin ice area that is lost due to ridging under converging conditions. In the middle of the year when melting dominates, the dependence on the ocean drag coefficient is significantly reduced. As expected, thermodynamic parameters become more important during this time as seen in the CICE results, which show a strong positive sensitivity response to visual ice albedo for May through October. The MPM results appear somewhat noisier; however, a positive sensitivity response is seen for the emissivity (ϵ), visual snow albedo ($\alpha_{snow,v}$), and visual ice albedo ($\alpha_{ice,v}$) in the middle of the year.

The standardized regression coefficients for total ice volume display interesting behavior and are similar for both codes (Figure 4.4.3). In the early part of the year from January to May, a strong positive response is seen for the fresh ice conductivity (k_0), which influences the growth of ice through the conductive flux. Until June, most other parameters show little if any influence on the total ice volume, but once the solar shortwave radiation input is significant the albedo parameters ($\alpha_{ice,v}, \alpha_{ice,i}, \alpha_{snow,v}$) and emissivity ($\epsilon$) begin to have an effect. Interestingly, in the case of both codes, the visual snow albedo has a greater influence in June and then decreases over the rest of the year. This is likely due to the fact that much of the ice is snow covered initially, but by later in the summer snow has melted thus exposing ice and increasing the importance of the visual ice albedo.

In the case of RMS ice speed the standardized regression coefficients display a fairly simple behavior for both codes (Figure 4.4.4). The RMS ice speed exhibits a strong negative sensitivity to the ice-ocean drag coefficient (c_w) throughout the year. This is entirely consistent with the formulation where a larger drag coefficient increases the drag on the ice and reduces the overall ice velocity. The other parameters, except perhaps for the ridging parameter μ in December for the CICE calculation, do not demonstrate any significant effects on the RMS ice speed.

The standardized regression coefficients for central Arctic ice thickness appear quite similar to the coefficients for total ice volume (Figure 4.4.5), which is not surprising since total ice volume is directly related to the thickness of the ice. As before, in the early part of the year a strong positive response to fresh ice conductivity (k_0) is seen and after June positive responses to albedo parameters ($\alpha_{ice,v}, \alpha_{ice,i}, \alpha_{snow,v}$) and emissivity ($\epsilon$) are seen. Also, the coefficients for the visual snow albedo again display an initial peak in June and a decrease over the summer, most likely due to the melting away of snow cover.

For the central Arctic ice speed the standardized regression coefficients display similar behavior to the coefficients for RMS ice speed (Figure 4.4.6). There is a strong negative response throughout the year to the ice-ocean drag coefficient (c_w) and minimal responses

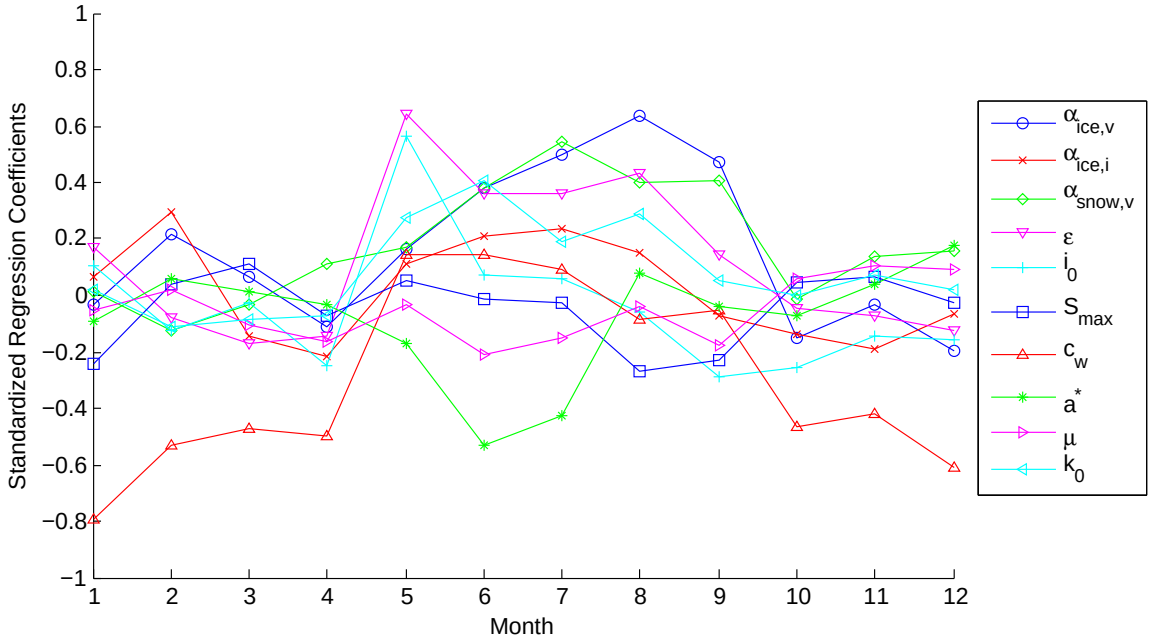

(a)

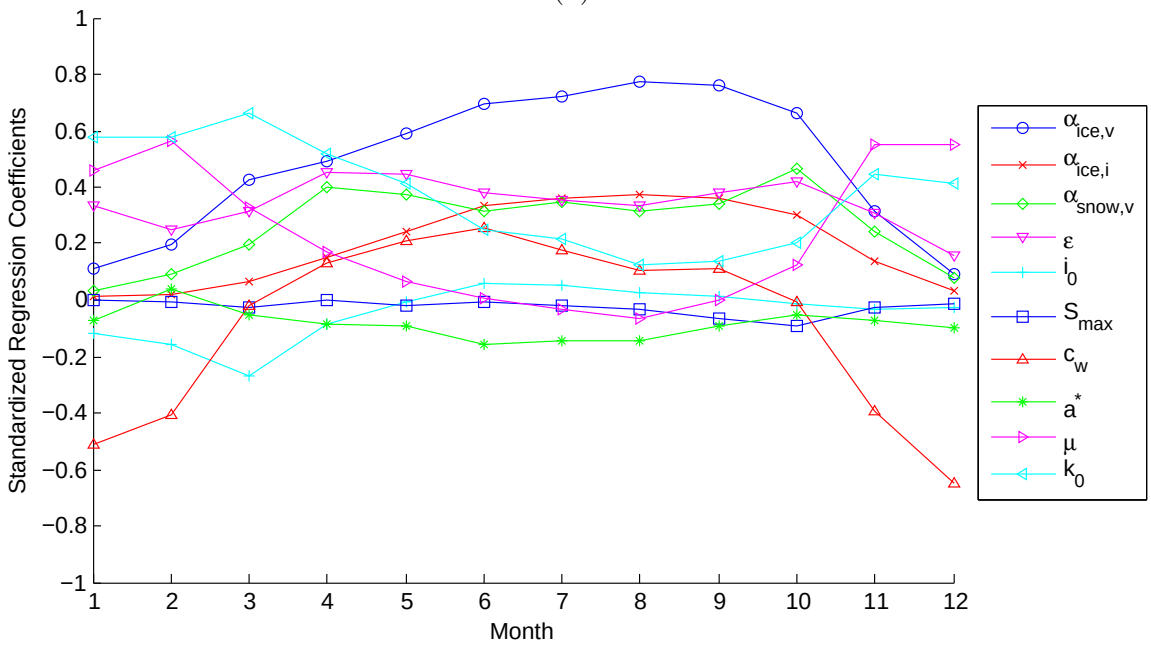

(b)

Figure 4.4.1: Standardized regression coefficients for total ice area with respect to the ten parameters for (a) MPM and (b) CICE.

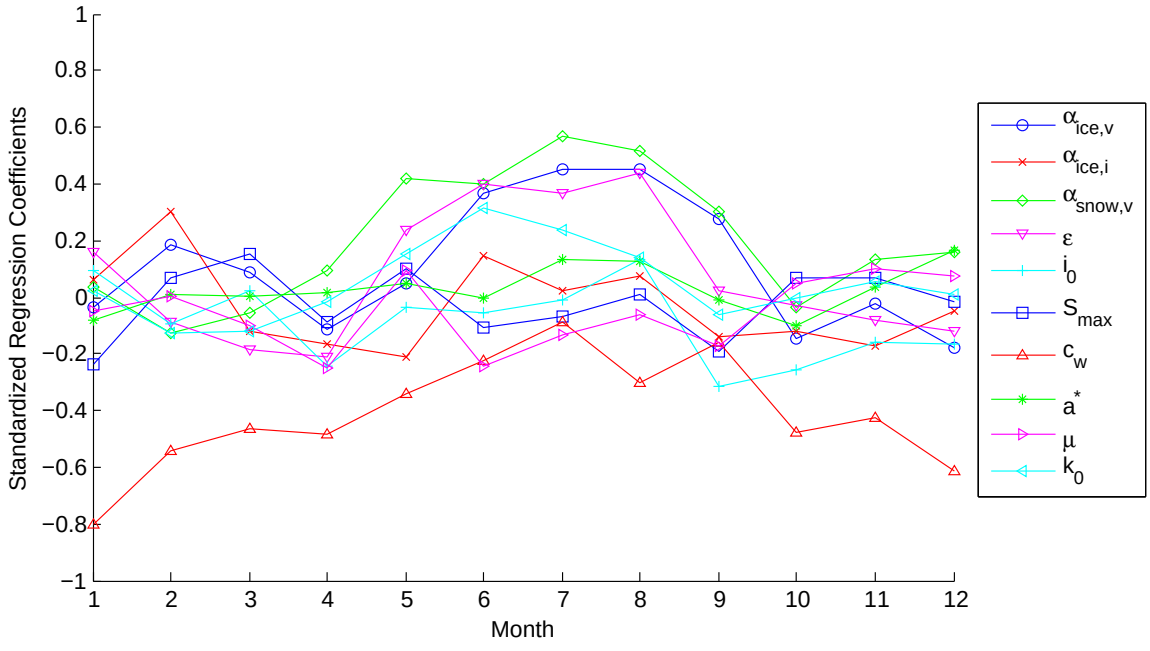

(a)

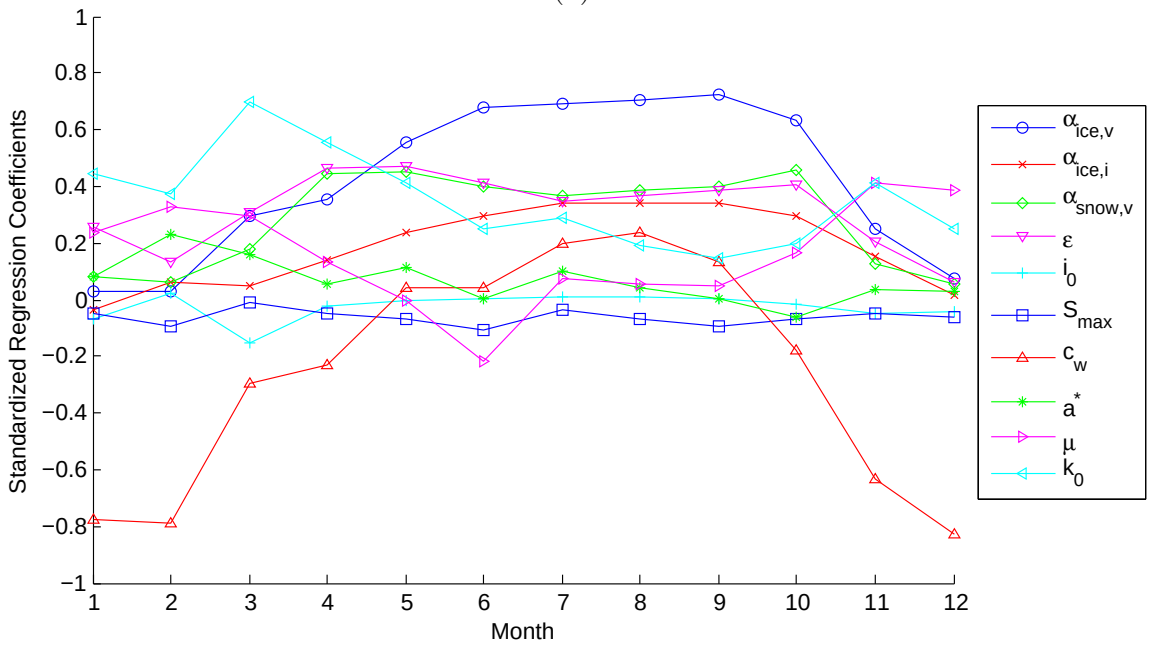

(b)

Figure 4.4.2: Standardized regression coefficients for total ice extent with respect to the ten parameters for (a) MPM and (b) CICE.

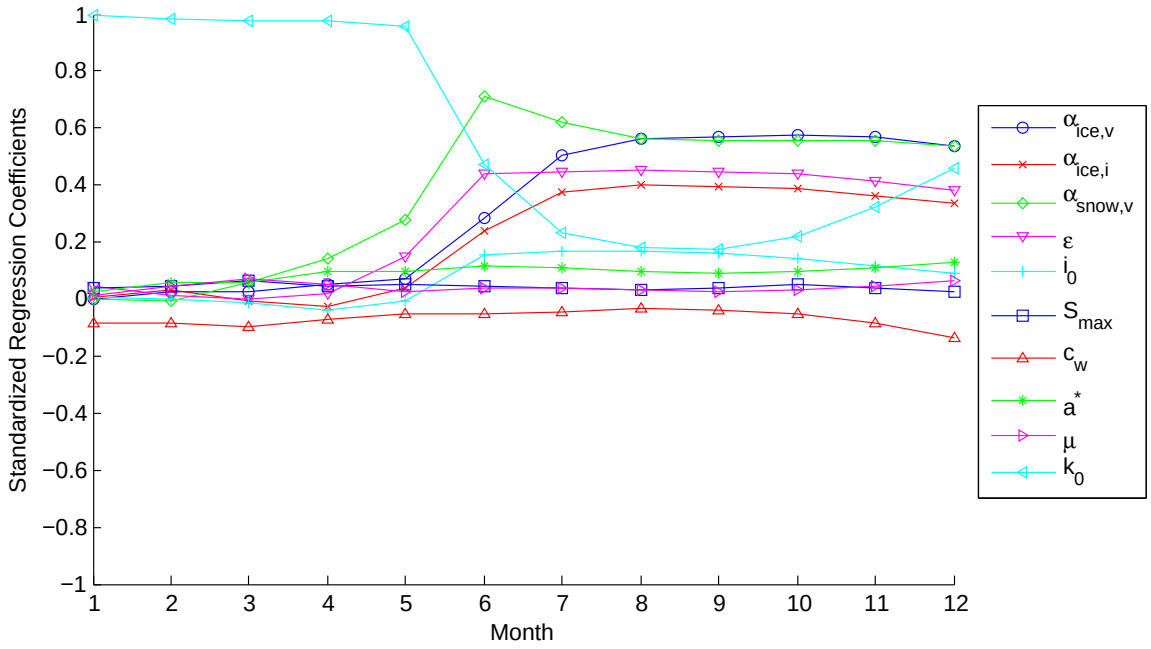

(a)

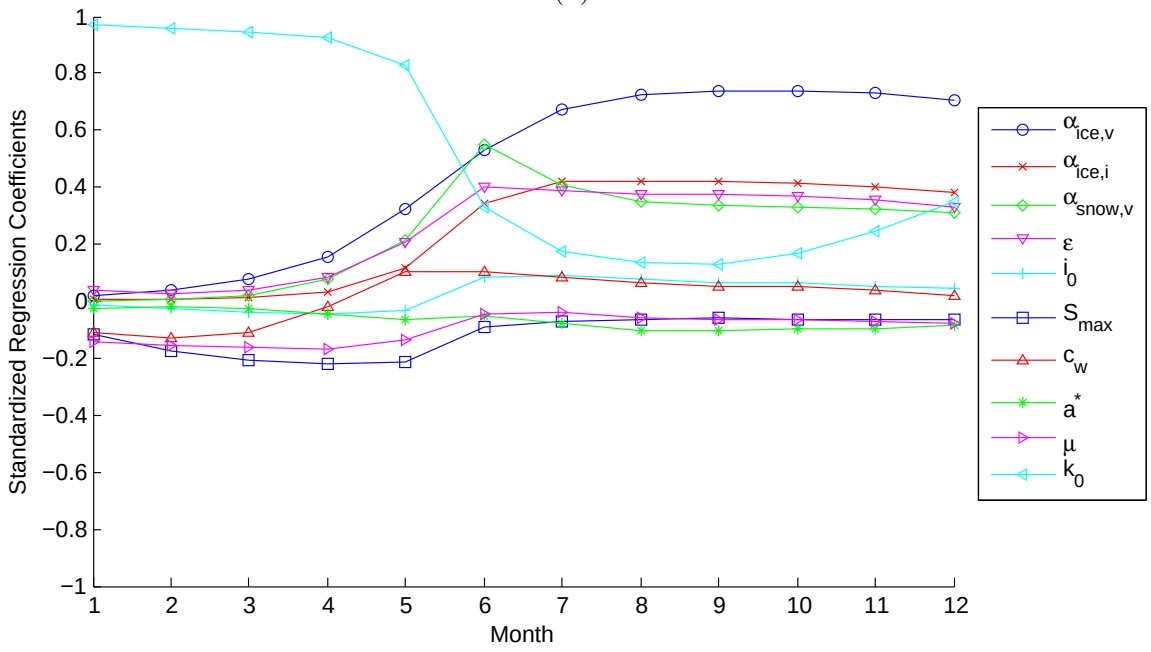

(b)

Figure 4.4.3: Standardized regression coefficients for total ice volume with respect to the ten parameters for (a) MPM and (b) CICE.

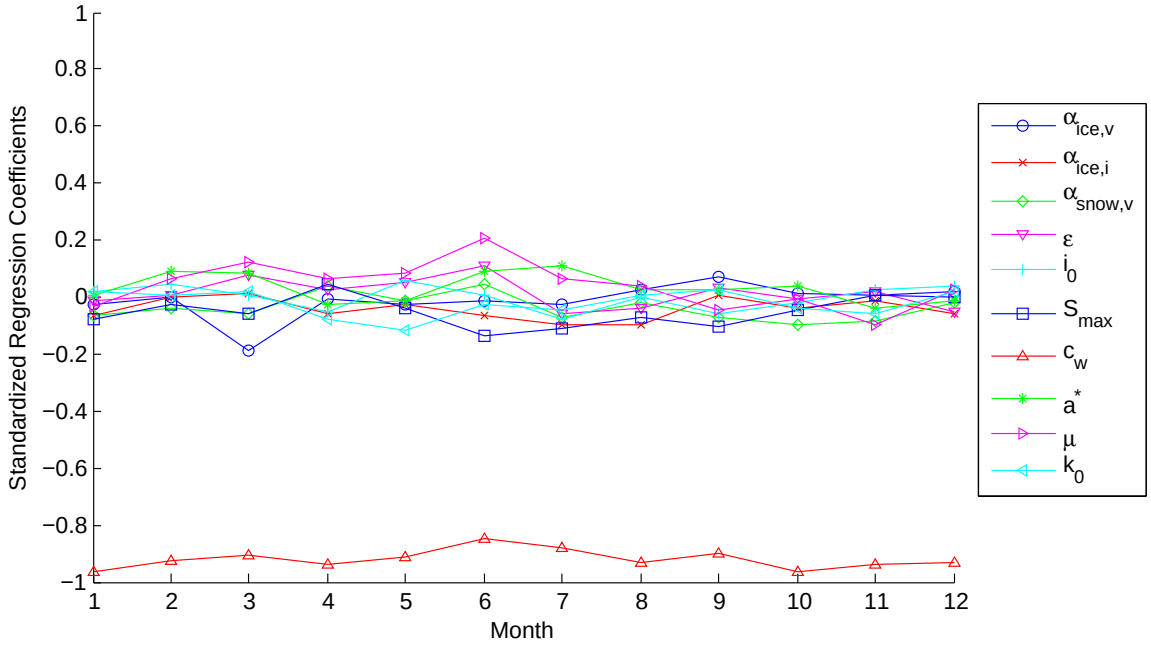

(a)

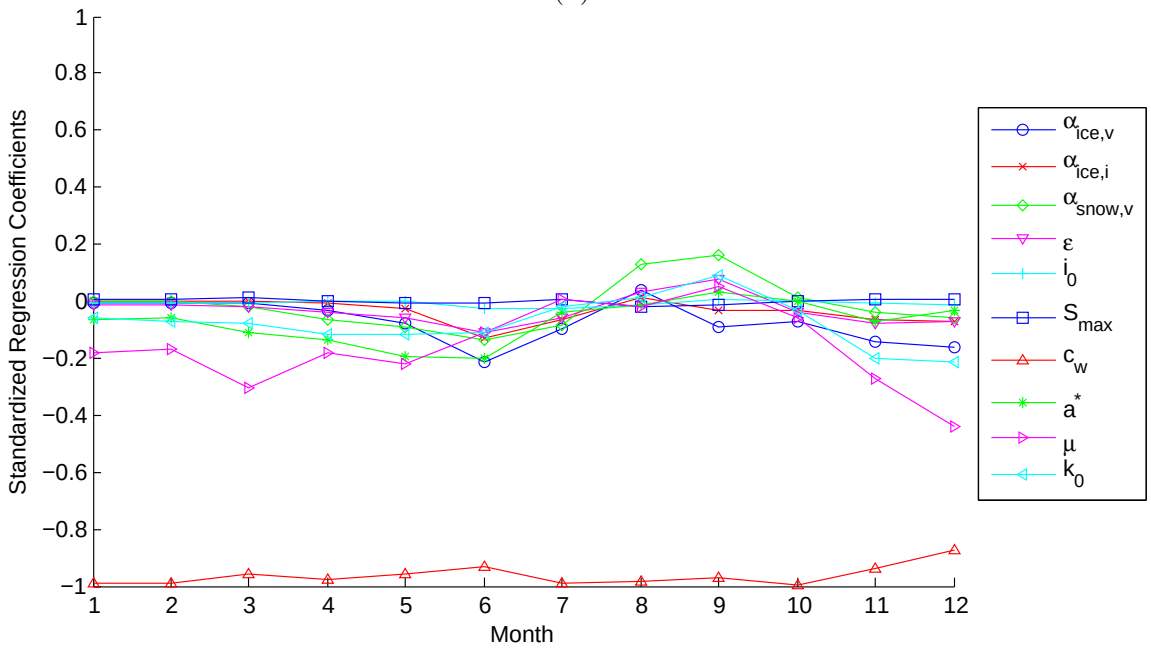

(b)

Figure 4.4.4: Standardized regression coefficients for RMS ice speed with respect to the ten parameters for (a) MPM and (b) CICE.

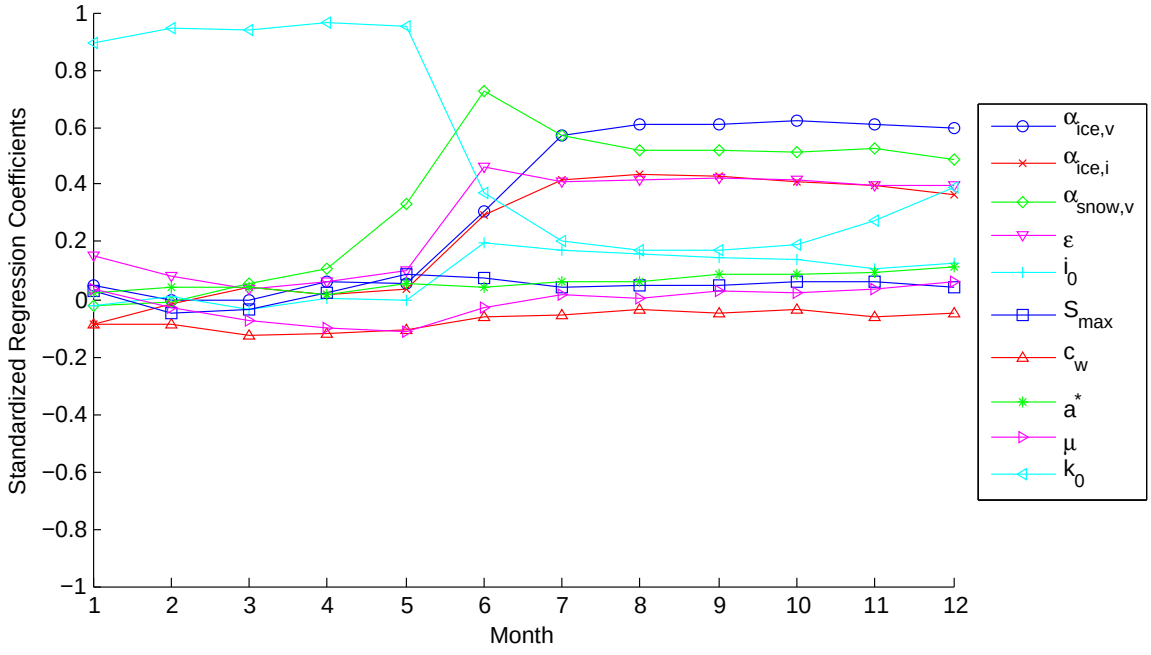

(a)

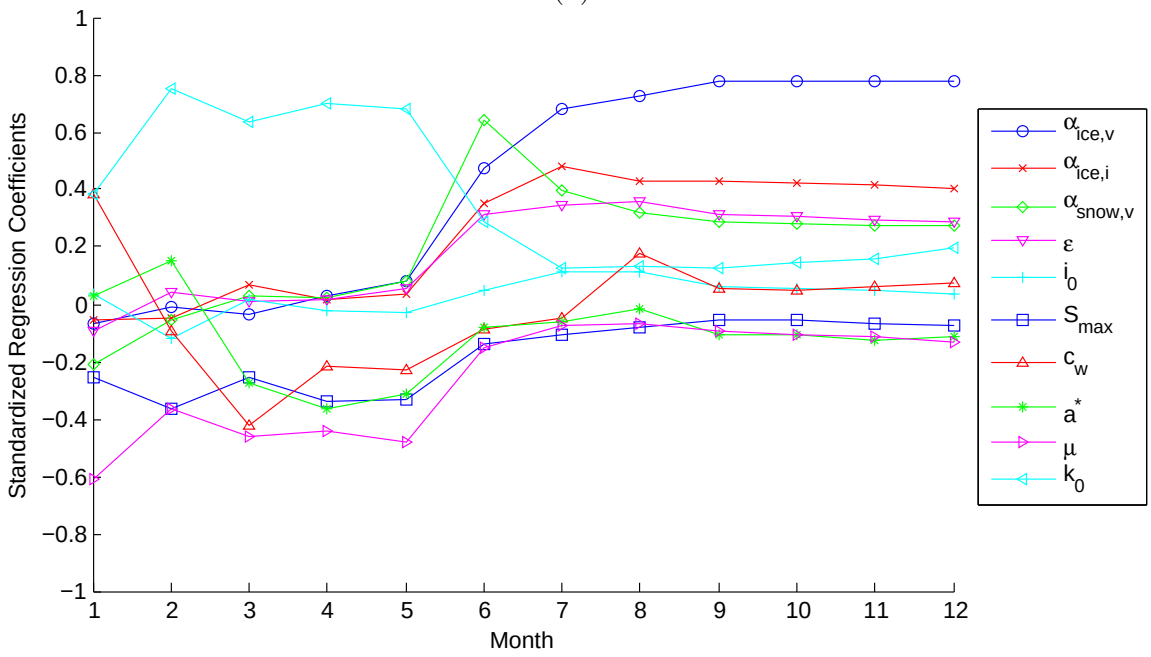

(b)

Figure 4.4.5: Standardized regression coefficients for central Arctic ice thickness with respect to the ten parameters for (a) MPM and (b) CICE.

for the other parameters. In the CICE case, the ridging parameter μ shows a negative response for March through May of the year.

Table 4.4.1: Three most significant parameters in CICE and MPM for A_{tot} ranked according to the magnitude of the standardized regression coefficient (in parentheses) for each month.

Month	A_{tot} CICE					
01	k_0	(0.582)	c_w	(-0.51)	μ	(0.450)
02	k_0	(0.576)	μ	(0.566)	c_w	(-0.408)
03	k_0	(0.665)	$\alpha_{ice,v}$	(0.425)	μ	(0.330)
04	k_0	(0.515)	$\alpha_{ice,v}$	(0.492)	ϵ	(0.450)
05	$\alpha_{ice,v}$	(0.591)	ϵ	(0.446)	k_0	(0.415)
06	$\alpha_{ice,v}$	(0.694)	ϵ	(0.377)	$\alpha_{ice,i}$	(0.334)
07	$\alpha_{ice,v}$	(0.722)	$\alpha_{ice,v}$	(0.360)	ϵ	(0.351)
08	$\alpha_{ice,v}$	(0.773)	$\alpha_{ice,v}$	(0.371)	ϵ	(0.333)
09	$\alpha_{ice,v}$	(0.758)	ϵ	(0.377)	$\alpha_{ice,v}$	(0.360)
10	$\alpha_{ice,v}$	(0.663)	$\alpha_{snow,i}$	(0.465)	ϵ	(0.422)
11	μ	(0.550)	k_0	(0.445)	c_w	(-0.390)
12	c_w	(-0.648)	μ	(0.550)	k_0	(0.411)
Month	A_{tot} MPM					
01	c_w	(-0.793)	S_{max}	(-0.244)	ϵ	(0.168)
02	c_w	(-0.534)	$\alpha_{ice,i}$	(0.297)	$\alpha_{ice,v}$	(0.213)
03	c_w	(-0.469)	ϵ	(-0.173)	$\alpha_{ice,i}$	(-0.146)
04	c_w	(-0.50)	i_0	(-0.252)	$\alpha_{ice,i}$	(-0.218)
05	ϵ	(0.640)	i_0	(0.564)	k_0	(0.277)
06	a^*	(-0.532)	k_0	(0.403)	$\alpha_{snow,i}$	(0.381)
07	$\alpha_{snow,i}$	(0.545)	$\alpha_{ice,v}$	(0.500)	a^*	(-0.423)
08	$\alpha_{ice,v}$	(0.634)	ϵ	(0.433)	$\alpha_{snow,i}$	(0.399)
09	$\alpha_{ice,v}$	(0.471)	$\alpha_{snow,i}$	(0.405)	i_0	(-0.289)
10	c_w	(-0.465)	i_0	(-0.256)	$\alpha_{ice,v}$	(0.147)
11	c_w	(-0.420)	$\alpha_{ice,i}$	(-0.190)	i_0	(-0.144)
12	c_w	(-0.607)	$\alpha_{ice,v}$	(-0.193)	a^*	(0.174)

Another way of looking at the data is provided in Tables 4.4.1–4.4.6, where the three most significant parameters, i.e., the parameters that have the highest impact on the given response function, are listed for each month with their associated standardized regression coefficients. Table 4.4.1 shows that the most significant parameter for total ice area (A_{tot}) often differs between MPM and CICE. This can also be seen in Figure 4.4.1 where even though the qualitative responses are similar for both codes parameter rankings may differ. From January to April the most significant parameter for the total ice area (A_{tot}) is k_0 in the case of CICE and is c_w in the case of MPM. During this time both codes show a negative response the ice-ocean drag coefficient (c_w), but for CICE the thermodynamic parameters, including k_0 produce a stronger response. During May, the total ice area is most sensitive to $\alpha_{ice,v}$ according to CICE; however, the SA results for MPM indicate that the total ice area

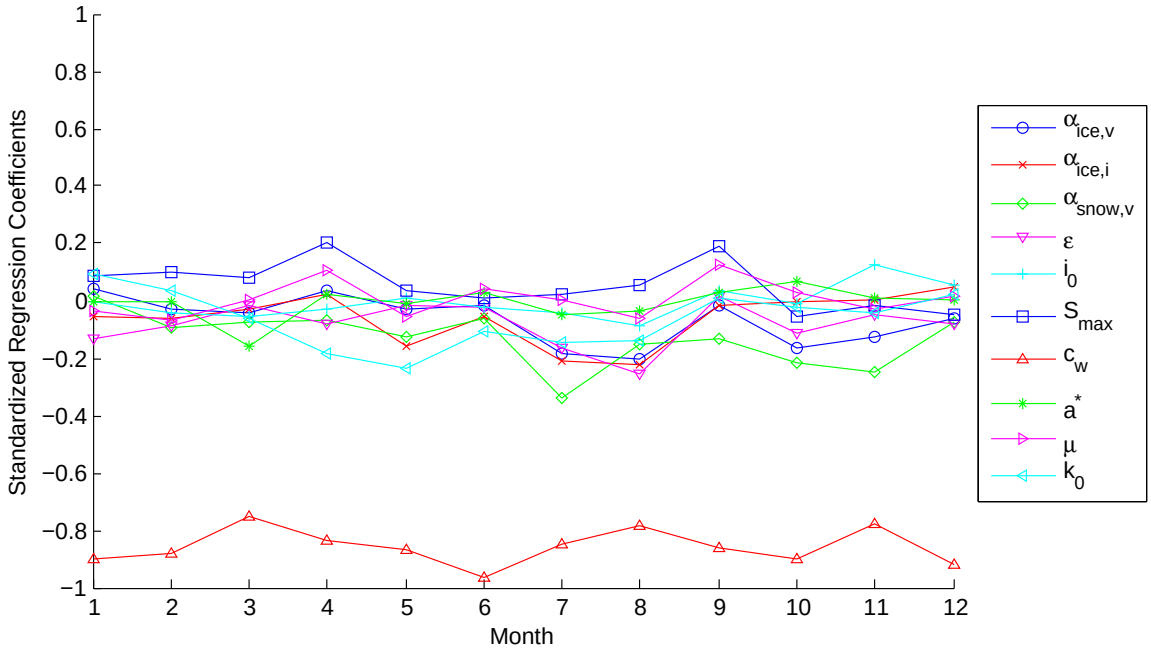

(a)

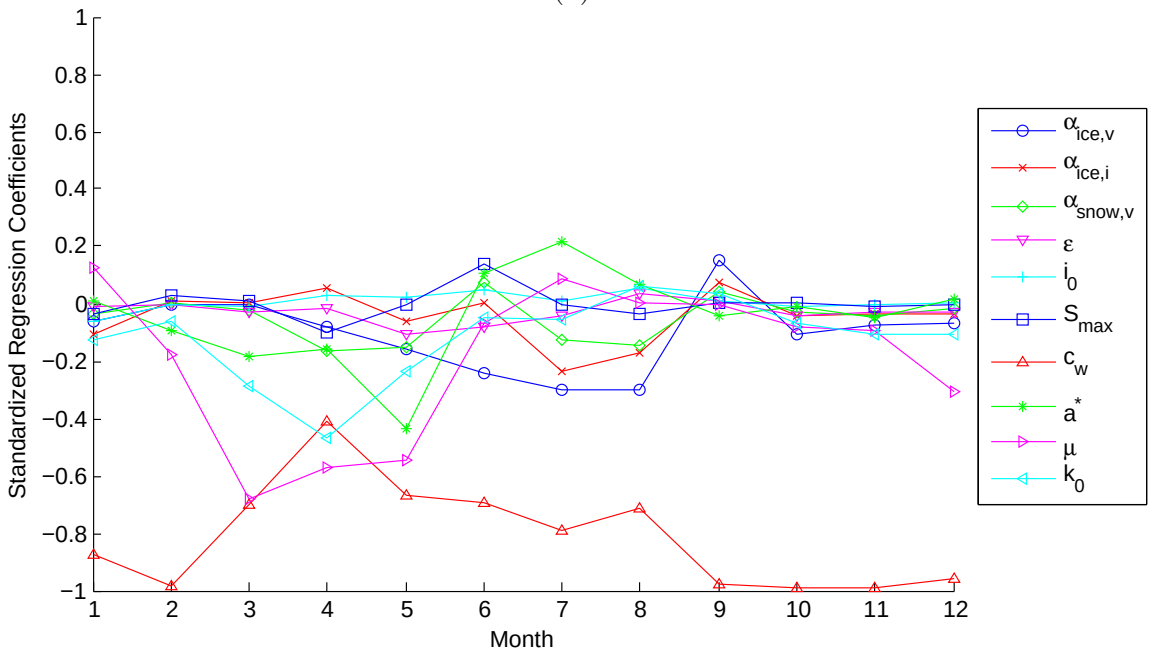

(b)

Figure 4.4.6: Standardized regression coefficients for central Arctic ice speed with respect to the ten parameters for (a) MPM and (b) CICE.

Table 4.4.2: Three most significant parameters in CICE and MPM for E_{tot} ranked according to the magnitude of the standardized regression coefficient (in parentheses) for each month.

Month	E_{tot} CICE					
01	c_w	(-0.776)	k_0	(0.446)	ϵ	(0.256)
02	c_w	(-0.788)	k_0	(0.372)	μ	(0.326)
03	k_0	(0.700)	ϵ	(0.310)	c_w	(-0.297)
04	k_0	(0.533)	ϵ	(0.466)	$\alpha_{snow,i}$	(-0.297)
05	$\alpha_{ice,v}$	(0.555)	ϵ	(0.469)	$\alpha_{snow,i}$	(0.449)
06	$\alpha_{ice,v}$	(0.681)	ϵ	(0.410)	$\alpha_{snow,i}$	(0.401)
07	$\alpha_{ice,v}$	(0.692)	$\alpha_{snow,i}$	(0.369)	ϵ	(0.348)
08	$\alpha_{ice,v}$	(0.707)	$\alpha_{snow,i}$	(0.385)	ϵ	(0.370)
09	$\alpha_{ice,v}$	(0.724)	$\alpha_{snow,i}$	(0.400)	ϵ	(0.389)
10	$\alpha_{ice,v}$	(0.630)	$\alpha_{snow,i}$	(0.458)	ϵ	(0.406)
11	c_w	(-0.633)	μ	(0.413)	k_0	(0.411)
12	c_w	(-0.827)	μ	(0.386)	k_0	(0.251)
Month	E_{tot} MPM					
01	c_w	(-0.801)	S_{max}	(-0.238)	ϵ	(-0.161)
02	c_w	(-0.543)	$\alpha_{ice,i}$	(0.302)	$\alpha_{ice,v}$	(-0.187)
03	c_w	(-0.463)	ϵ	(-0.183)	S_{max}	(0.155)
04	c_w	(-0.486)	μ	(-0.252)	i_0	(-0.244)
05	$\alpha_{snow,i}$	(0.416)	c_w	(-0.343)	ϵ	(-0.235)
06	ϵ	(-0.400)	$\alpha_{snow,i}$	(0.397)	$\alpha_{ice,v}$	(0.369)
07	$\alpha_{snow,i}$	(0.571)	$\alpha_{ice,v}$	(-0.451)	ϵ	(-0.367)
08	$\alpha_{snow,i}$	(0.518)	$\alpha_{ice,v}$	(-0.451)	ϵ	(-0.440)
09	i_0	(-0.314)	$\alpha_{snow,i}$	(0.300)	$\alpha_{ice,v}$	(-0.278)
10	c_w	(-0.474)	i_0	(-0.256)	$\alpha_{ice,v}$	(-0.143)
11	c_w	(-0.420)	$\alpha_{ice,i}$	(-0.171)	i_0	(-0.157)
12	c_w	(-0.613)	$\alpha_{ice,v}$	(-0.178)	i_0	(-0.167)

is most sensitive to ϵ. For June the total ice area continues to be most sensitive to $\alpha_{ice,v}$ according to CICE but it changes sensitivity to a^* for MPM. This is the only point where the ridging parameter a^* is the most significant and, in general, it does not have a significant effect on the response functions. For August, September and December both CICE and MPM show sensitivity of the total ice area to the same parameters: $\alpha_{ice,v}$ for August and September and c_w during December. For MPM c_w is the most significant parameter for the total ice area in October and November, as well. The SA for CICE shows different results, however. In October, the total ice area is most sensitive to $\alpha_{ice,v}$ and in November the sensitivity changes to μ. Some of the differences between the responses for the two codes may be due to the use of an ocean mixed-layer model in CICE. This algorithm allows for changes in SST due to thermodynamic fluxes through the ice, which may have a strong influence on where ice grows and melts thereby changing the ice area and extent.

Table 4.4.3: Three most significant parameters in CICE and MPM for V_{tot} ranked according to the magnitude of the standardized regression coefficient (in parentheses) for each month.

Month	V_{tot} CICE					
01	k_0	(0.97)	μ	(-0.143)	S_{max}	(-0.115)
02	k_0	(0.96)	S_{max}	(-0.174)	μ	(-0.153)
03	k_0	(0.94)	S_{max}	(-0.204)	μ	(-0.163)
04	k_0	(0.926)	S_{max}	(-0.220)	μ	(0.167)
05	k_0	(0.83)	$\alpha_{ice,v}$	(0.332)	S_{max}	(-0.125)
06	$\alpha_{snow,i}$	(0.55)	$\alpha_{ice,v}$	(0.527)	ϵ	(0.401)
07	$\alpha_{ice,v}$	(0.68)	$\alpha_{ice,i}$	(0.424)	$\alpha_{snow,i}$	(0.409)
08	$\alpha_{ice,v}$	(0.73)	$\alpha_{ice,i}$	(0.422)	ϵ	(0.378)
09	$\alpha_{ice,v}$	(0.74)	$\alpha_{ice,i}$	(0.418)	ϵ	(0.375)
10	$\alpha_{ice,v}$	(0.74)	$\alpha_{ice,i}$	(0.413)	ϵ	(0.368)
11	$\alpha_{ice,v}$	(0.728)	$\alpha_{ice,i}$	(0.399)	ϵ	(0.353)
12	$\alpha_{ice,v}$	(0.705)	$\alpha_{ice,i}$	(0.380)	k_0	(0.352)
Month	V_{tot} MPM					
01	k_0	(0.996)	c_w	(-0.086)	ϵ	(0.045)
02	k_0	(0.980)	c_w	(-0.087)	a^*	(0.058)
03	k_0	(0.979)	c_w	(-0.099)	μ	(0.070)
04	k_0	(0.979)	$\alpha_{snow,i}$	(0.140)	a^*	(0.098)
05	k_0	(0.954)	$\alpha_{snow,i}$	(0.277)	ϵ	(0.147)
06	$\alpha_{snow,i}$	(0.714)	k_0	(0.469)	ϵ	(0.439)
07	$\alpha_{snow,i}$	(0.622)	$\alpha_{ice,v}$	(0.502)	ϵ	(0.444)
08	$\alpha_{snow,i}$	(0.561)	$\alpha_{ice,v}$	(0.560)	ϵ	(0.456)
09	$\alpha_{ice,v}$	(0.572)	$\alpha_{snow,i}$	(0.560)	ϵ	(0.449)
10	$\alpha_{ice,v}$	(0.577)	$\alpha_{snow,i}$	(0.559)	ϵ	(0.437)
11	$\alpha_{ice,v}$	(0.569)	$\alpha_{snow,i}$	(0.557)	ϵ	(0.415)
12	$\alpha_{ice,v}$	(0.536)	$\alpha_{snow,i}$	(0.560)	k_0	(0.456)

The SA results presented in Table 4.4.2 compare the ranking in sensitivity of the the response E_{tot} for CICE and MPM with respect to the top three most significant models parameters. For January, February, November and December, both codes show highest sensitivity of E_{tot} to the ice-ocean drag coefficient (c_w). MPM's E_{tot} continues to show highest sensititvity to c_w during March and April and October; however, CICE's E_{tot} shows highest sensitivity to k_0 for March and April and to $\alpha_{ice,v}$ for October. For the rest of the year, the most significant parameter for E_{tot} calculated by CICE is $\alpha_{ice,v}$; for MPM's E_{tot} significant parameters are $\alpha_{snow,i}$, ϵ and i_0. It is interesting to note that the second and third most significant parameters show relatively high sensitivity values of the E_{tot} for both CICE and MPM for some months. For example, for June, the MPM's E_{tot} response demonstrates almost uniform sensitivity to ϵ, $\alpha_{snow,i}$, $\alpha_{ice,v}$. Similar observation holds during May for CICE: the E_{tot} is almost equally sensitive to $\alpha_{ice,v}$, ϵ and $\alpha_{snow,i}$.

Table 4.4.4: Three most significant parameters in CICE and MPM for $\mathbf{v}_{rms}$ ranked according to the magnitude of the standardized regression coefficient (in parentheses) for each month.

Month	$\mathbf{v}_{rms}$ CICE					
01	c_w	(-0.989)	μ	(-0.179)	a^*	(-0.64)
02	c_w	(-0.991)	μ	(-0.167)	k_0	(-0.072)
03	c_w	(-0.960)	μ	(-0.303)	a^*	(-0.122)
04	c_w	(-0.977)	μ	(-0.184)	a^*	(-0.133)
05	c_w	(-0.957)	μ	(-0.218)	a^*	(-0.193)
06	c_w	(-0.932)	$\alpha_{ice,v}$	(-0.214)	a^*	(-0.198)
07	c_w	(-0.989)	$\alpha_{ice,v}$	(-0.099)	$\alpha_{snow,i}$	(-0.081)
08	c_w	(-0.985)	$\alpha_{snow,i}$	(-0.129)	$\alpha_{ice,v}$	(-0.039)
09	c_w	(-0.969)	$\alpha_{snow,i}$	(-0.159)	$\alpha_{ice,v}$	(-0.09)
10	c_w	(-0.996)	μ	(-0.073)	$\alpha_{ice,v}$	(-0.06)
11	c_w	(-0.941)	μ	(-0.271)	k_0	(-0.200)
12	c_w	(-0.876)	μ	(-0.441)	k_0	(-0.216)
Month	$\mathbf{v}_{rms}$ MPM					
01	c_w	(-0.964)	S_{max}	(-0.076)	$\alpha_{ice,i}$	(-0.067)
02	c_w	(-0.926)	a^*	(0.092)	μ	(0.066)
03	c_w	(-0.904)	$\alpha_{ice,v}$	(-0.189)	μ	(0.121)
04	c_w	(-0.939)	k_0	(-0.079)	μ	(0.066)
05	c_w	(-0.915)	k_0	(-0.177)	μ	(0.082)
06	c_w	(-0.846)	μ	(0.206)	S_{max}	(-0.133)
07	c_w	(-0.883)	S_{max}	(-0.133)	a^*	(0.108)
08	c_w	(-0.929)	$\alpha_{ice,i}$	(-0.099)	S_{max}	(-0.074)
09	c_w	(-0.898)	S_{max}	(-0.102)	$\alpha_{snow,i}$	(-0.073)
10	c_w	(-0.966)	$\alpha_{snow,i}$	(-0.094)	S_{max}	(-0.045)
11	c_w	(-0.939)	μ	(-0.095)	$\alpha_{snow,i}$	(-0.086)
12	c_w	(-0.932)	$\alpha_{ice,i}$	(-0.059)	ϵ	(-0.054)

The SA results in Table 4.4.3 show more consistent results for the two codes. From the SA results in Table 4.4.3, the most significant parameter from January to May is the fresh ice conductivity (k_0) for both CICE and MPM. For June, the SA results for CICE and MPM indicate that the total ice volume is most sensitive to near-infrared snow albedo $\alpha_{snow,i}$. For July and August the results for CICE shows that the total ice volume is most sensitive to visual ice albedo $\alpha_{ice,v}$. However, MPM results show that the total ice volume is most sensitive to near-infrared ice albedo $\alpha_{ice,i}$. From September to December the results for both codes show consistently that the total ice volume is most sensitive to visual ice albedo $\alpha_{snow,v}$. Overall, the first five months are dominated by fresh ice conductivity (k_0) and the final seven months by one of the three albedo parameters. This result implies that the total ice volume is primarily influenced by the thermodynamic flux balance at the ice-atmosphere boundary.

Table 4.4.5: Three most significant parameters in CICE and MPM for h_{CA} ranked according to the magnitude of the standardized regression coefficient (in parentheses) for each month.

Month	h_{CA} CICE					
01	μ	(-0.607)	c_w	(0.238)	k_0	(0.382)
02	k_0	(0.752)	μ	(-0.365)	S_{max}	(-0.362)
03	k_0	(0.633)	μ	(-0.459)	c_w	(-0.44)
04	k_0	(0.697)	μ	(-0.440)	a^*	(-0.362)
05	k_0	(0.679)	μ	(-0.479)	S_{max}	(-0.332)
06	$\alpha_{snow,i}$	(0.694)	$\alpha_{ice,v}$	(0.474)	$\alpha_{ice,i}$	(0.351)
07	$\alpha_{ice,v}$	(0.679)	$\alpha_{ice,i}$	(0.483)	$\alpha_{snow,i}$	(0.396)
08	$\alpha_{ice,v}$	(0.725)	$\alpha_{ice,i}$	(0.430)	ϵ	(0.355)
09	$\alpha_{ice,v}$	(0.778)	$\alpha_{ice,i}$	(0.429)	ϵ	(0.313)
10	$\alpha_{ice,v}$	(0.779)	$\alpha_{ice,i}$	(0.425)	ϵ	(0.304)
11	$\alpha_{ice,v}$	(0.779)	$\alpha_{ice,i}$	(0.418)	ϵ	(0.294)
12	$\alpha_{ice,v}$	(0.778)	$\alpha_{ice,i}$	(0.403)	ϵ	(0.286)
Month	h_{CA} MPM					
01	k_0	(0.89)	ϵ	(0.148)	$\alpha_{ice,i}$	(-0.089)
02	k_0	(0.945)	c_w	(-0.088)	ϵ	(0.079)
03	k_0	(0.940)	c_w	(-0.127)	μ	(-0.127)
04	k_0	(0.962)	c_w	(-0.121)	$\alpha_{snow,i}$	(0.109)
05	k_0	(0.949)	$\alpha_{snow,i}$	(0.335)	μ	(0.113)
06	$\alpha_{snow,i}$	(0.726)	ϵ	(0.604)	k_0	(0.369)
07	$\alpha_{snow,i}$	(0.573)	$\alpha_{ice,v}$	(0.57)	$\alpha_{ice,i}$	(0.419)
08	$\alpha_{ice,v}$	(0.612)	$\alpha_{snow,i}$	(0.518)	$\alpha_{ice,i}$	(0.435)
09	$\alpha_{ice,v}$	(0.608)	$\alpha_{snow,i}$	(0.520)	$\alpha_{ice,i}$	(0.427)
10	$\alpha_{ice,v}$	(0.622)	$\alpha_{snow,i}$	(0.512)	ϵ	(0.413)
11	$\alpha_{ice,v}$	(0.611)	$\alpha_{snow,i}$	(0.526)	ϵ	(0.398)
12	$\alpha_{ice,v}$	(0.600)	$\alpha_{snow,i}$	(0.485)	ϵ	(0.397)

The results in Table 4.4.4 consistently show that the most significant parameter for the RMS ice speed during the entire year for both CICE and MPM is the ice-ocean drag parameter (c_w). In the case of CICE the second most important parameter is an albedo parameter from June through September and the ridging coefficient μ during the rest of the year, which suggests that thermodynamic parameters are more important during the melt season and ridging parameters are more important during the remainder of the year. There is more variability in the second and third most important parameter for MPM, but these parameters all have standardized regression coefficients with absolute values generally less than 0.2 and often less than 0.1, which makes them much less significant.

The results in Table 4.4.5 for central Arctic ice thickness display similar behavior to the results for total ice volume. For the first five months of year, the central Arctic ice thickness sensitivity is dominated by the fresh ice conductivity (k_0) and the rest of the year by albedo

Table 4.4.6: Three most significant parameters in CICE and MPM for $\mathbf{v}_{CA}$ ranked according to the magnitude of the standardized regression coefficient (in parentheses) for each month.

Month	$\mathbf{v}_{CA}$ CICE					
01	c_w	(-0.872)	μ	(-0.126)	k_0	(-0.125)
02	c_w	(-0.986)	μ	(-0.178)	a^*	(-0.091)
03	c_w	(-0.698)	μ	(-0.680)	k_0	(-0.289)
04	μ	(-0.569)	k_0	(-0.466)	c_w	(0.410)
05	c_w	(-0.670)	μ	(-0.542)	a^*	(-0.434)
06	c_w	(-0.694)	$\alpha_{ice,v}$	(-0.241)	S_{max}	(0.138)
07	c_w	(-0.793)	$\alpha_{ice,v}$	(-0.303)	$\alpha_{ice,i}$	(-0.237)
08	c_w	(-0.715)	$\alpha_{ice,v}$	(-0.303)	$\alpha_{ice,i}$	(-0.173)
09	c_w	(-0.976)	$\alpha_{ice,v}$	(-0.149)	$\alpha_{ice,i}$	(-0.176)
10	c_w	(-0.993)	$\alpha_{ice,v}$	(-0.104)	μ	(-0.080)
11	c_w	(-0.987)	k_0	(-0.107)	μ	(-0.095)
12	c_w	(-0.956)	μ	(-0.307)	k_0	(-0.108)
Month	$\mathbf{v}_{CA}$ MPM					
01	c_w	(-0.900)	ϵ	(-0.134)	k_0	(-0.093)
02	c_w	(-0.878)	S_{max}	(0.3101)	$\alpha_{snow,i}$	(-0.094)
03	c_w	(-0.749)	a^*	(-0.155)	S_{max}	(0.081)
04	c_w	(-0.833)	S_{max}	(-0.201)	k_0	(-0.182)
05	c_w	(-0.869)	k_0	(-0.235)	$\alpha_{ice,i}$	(0.156)
06	c_w	(-0.964)	k_0	(0.140)	$\alpha_{snow,i}$	(0.060)
07	c_w	(-0.846)	$\alpha_{snow,i}$	(0.341)	$\alpha_{ice,i}$	(0.210)
08	c_w	(-0.785)	ϵ	(0.258)	$\alpha_{ice,i}$	(0.220)
09	c_w	(-0.846)	S_{max}	(0.189)	$\alpha_{snow,i}$	(-0.193)
10	c_w	(-0.903)	$\alpha_{snow,i}$	(0.217)	$\alpha_{ice,v}$	(-0.161)
11	c_w	(-0.777)	$\alpha_{snow,i}$	(0.284)	$\alpha_{ice,v}$	(-0.128)
12	c_w	(-0.918)	$\alpha_{ice,v}$	(-0.083)	i_0	(-0.077)

parameters. The second and third most important parameters for June through December for both CICE and MPM with respect to central Arctic ice thickness are either emissivity (ϵ) or one of the albedos indicating that thermodynamic parameters have the most significant effect during this time of year.

The results in Table 4.4.6 for central Arctic ice speed are similar to the results for RMS ice speed in that the most significant parameter during the entire year for both CICE and MPM is the ice-ocean drag parameter (c_w). Central Arctic ice speed demonstrates high sensitivity (*i.e.*, absolute value of standardized regression coefficient greater than 0.5) to μ during March and May for CICE, but for MPM the top three most significant parameters are all thermodynamic parameters and do not include μ.

In order to visualize the amount of variation over the fifty samples in selected responses,

the mean of total ice volume, total ice area, and RMS ice speed over the year for fifty samples are shown in Figure 4.4.7 by the black line with two standard deviations from the mean indicated by the blue lines. Qualitatively, the seasonal cycle of ice volume and area are similar for the CICE and MPM codes. In the case of the volume, CICE exhibits more variation over the season with a maximum of 3.72×10^{13} m^3 and a minimum of 1.13×10^{13} m^3 compared to the MPM maximum of 3.63×10^{13} m^3 and minimum of 1.44×10^{13} m^3.

In the case of total ice area, the MPM code exhibits more spread in the samples throughout the majority of the year, although near the time of minimum ice extent it displays less variation than CICE. The lack of variation at the minimum may be due to the ocean mixed layer model in CICE that allows SST to vary based on radiative and other fluxes passing to the upper layer of the ocean. The SST is used to calculate the ocean flux, which is important for determining whether ice is melting or growing at a particular location. Note, however, that although the CICE set of calculations displays a large spread in total sea ice area in the summer, at the end of the year this spread has reduced significantly. This suggests that variations in sea ice area due to physical parameter perturbations when using a more realistic mixed-layer formulation are not cumulative over multiple years.

The velocity in both cases is somewhat noisy, which is likely due to the fact that the ice was started from rest at the beginning of the year. Using a multi-year initialization that starts from a point of near equilibrium may reduce the noise. However, the standard deviations of the sample velocities are not large. This is consistent with the observation that most of the parameters chosen for the sensitivity study do not have a significant effect on velocity. In future research it would be interesting to compare the relative importance of rheological parameters with the ice-ocean drag coefficient on the velocity to determine which has a stronger effect.

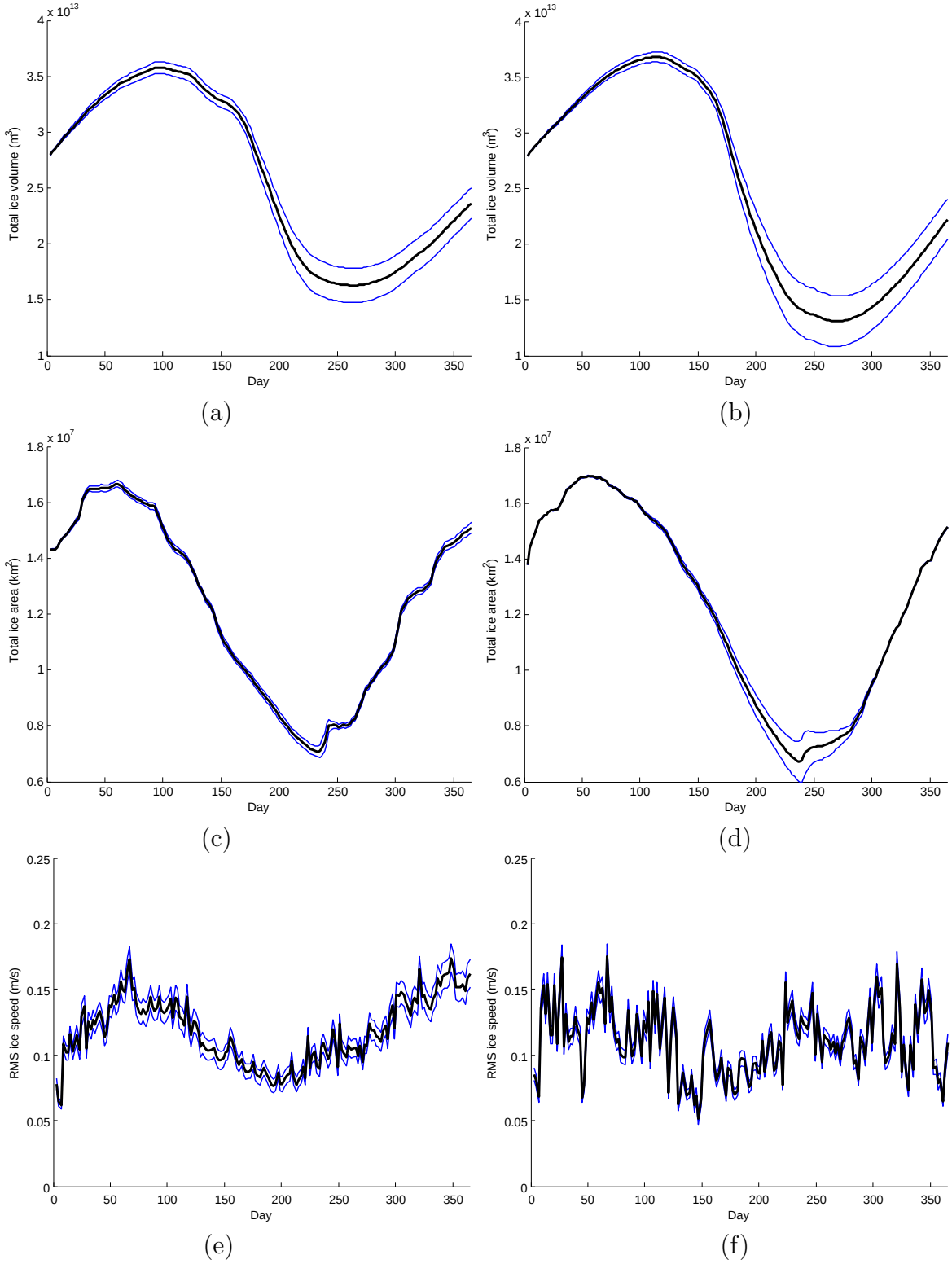

Figure 4.4.7: The seasonal cycle showing the mean (black) and two-sigma bounds (blue) of (a) MPM ice volume, (b) CICE ice volume, (c) MPM ice area, (d) CICE ice area, (e) MPM RMS ice speed, (f) CICE RMS ice speed, for 50 Latin hypercube samples.

Chapter 5

Conclusions

A new sea ice model has been developed for basin-scale calculations of the Arctic ocean that combines a new anisotropic constitutive model with a particle-in-cell type numerical solution of the ice dynamics governing equations. We compare this model to the state-of-the-art LANL CICE code in a single year simulation of the Arctic basin. Although, the ice thickness distribution and velocity at the end of the one year simulation differ substantially between the codes, the response of each code to perturbations in a set of ten dynamic and thermodynamic parameters is quite similar.

Of the ten parameters of interest, the maximum salinity (S_{max}) does not have significant influence on any of the response functions evaluated in this study and could probably be neglected in future studies. The ridging parameters (a^*, μ) also do not seem to have a significant influence on most of the response functions and could likely also be neglected in future studies. Interestingly, the thickness and volume show a strong positive response to fresh ice conductivity (k_0) in the first part of the year, but, as expected, the albedo parameters ($\alpha_{ice,v}, \alpha_{ice,i}, \alpha_{snow,v}$) become more significant than the conductivity between May and June. It is likely that the conductivity would not show such a significantly higher response in the early part of the year over a multi-year simulation since the changes in thickness and volume due to albedo perturbations would be cumulative over multiple years. Unsurprisingly, the velocity-related functions show strong negative responses to the ice-ocean drag coefficient (c_w). It is likely that only rheological parameters and ice-atmosphere drag parameters would have produced as significant of an effect. Overall, the data show that volume and thickness are strongly dependent on albedo and other thermodynamic parameters, ice area and extent are strongly dependent on dynamic parameters in the winter months and on thermodynamic parameters in the summer months, and the ice velocity is strongly dependent on only one of the dynamic parameters (c_w).

This study focused on the variability of output response functions of each code to changes in physical parameters within the models. In should be noted that the ocean and atmospheric data for these simulations were prescribed and it is likely that running the same calculations with a fully coupled atmosphere and ocean model would produce different results due to feedback effects between the ice and atmosphere and ice and ocean. An additional limitation was introduced by initializing the ice in both codes from rest. In future work, a similar multi-parameter study could be done from a more realistic intialized state. However, the simple initialization was very useful for providing an identical initial state for both codes that

allowed a direct comparison over time.

As part of our future work, we will continue to investigate sensitivity of both codes with respect to the model parameters. Our first step will be to rerun the SA considering other methods, such as response surface approximations to the original models considering higher than the first order terms, variance based methods and Bayesian SA and will compare the results across these different SA techniques. Once the most significant parameters are confirmed, we will propagate uncertainty through the models by varying only those parameters determined to be significant. We will then compare the variability ranges in the response function for the reduced and full order analysis. The goal will be to determine how well the smaller number of significant parameters can approximate the overall variability in the responses produced when all ten parameters are varied simultaneously. This analysis will give useful information on what the actual dimension of the problem space is and will be very useful for development of reliable, computationally efficient and scalable uncertainty quantification methodology for future high-fidelity arctic sea ice models predictions in terms of best estimates and uncertainty ranges.

References

[1] B. M. Adams, W. J. Bohnhoff, K. R. Dalbey, J. P. Eddy, M. S. Eldred, D. M. Gay, K. Haskell, P. D. Hough, and L. P. Swiler. DAKOTA, a multilevel parallel object-oriented framework for design optimization, parameter estimation, uncertainty quantification, and sensitivity analysis: Version 5.0 user's manual. Technical Report SAND2010-2183, Sandia National Laboratories, 2009.

[2] C. M. Bitz and W. H. Lipscomb. An energy-conserving thermodynamic model of sea ice. *Journal of Geophysical Research*, 104(C7):15669–15677, 1999.

[3] D. Budikova. Role of Arctic sea ice in global atmospheric circulation: A review. *Global and Planetary Change*, 68:149–163, 2009.

[4] W. L. Chapman, W. J. Welch, K. P Bowman, J. Sacks, and J. E. Walsh. Arctic sea ice variability: model sensitivities and a multidecadal simulation. *Journal of Geophysical Research*, 99(C1):919–935, 1994.

[5] M. Coon, R. Kwok, G. Levy, M. Pruis, H. Schreyer, and D. Sulsky. Arctic ice dynamics experiment AIDJEX assumptions revisited and found inadequate. *Journal of Geophysical Research*, 112:C11S90, 2007.

[6] K. Dethloff, A. Rinke, A. Benkel, M. Koltzow, E Sokolova, S. Kumar Saha, D. Handorf, W. Dorn, B. Rockel, H. von Storch, J. E. Haugen, L. P Roed, E Roeckner, J. H. Christensen, and M. Stendel. A dynamic link between the Arctic and the global climate system. *Geophysical Research Letters*, 33:L03703, 2006.

[7] J. M. N. T. Gray and L. W. Morland. A two-dimensional model for the dynamics of sea ice. *Philosophical Transactions: Physical Sciences and Engineering*, 347(1682):219–290, 1994.

[8] J. C. Helton. Uncertainty and sensitivity analysis techniques for use in performance assessment for radioactive waste disposal. *Reliability Engineering and System Safety*, 42:327–367, 1993.

[9] W. D. Hibler. A dynamic thermodynamic sea ice model. *Journal of Physical Oceanography*, 9:815–845, 1979.

[10] D. M. Holland, L. A. Mysak, D. K Manak, and J. M. Oberhuber. Sensitivity study of a dynamic thermodynamic sea ice model. *Journal of Geophysical Research*, 98(C2):2561–2586, 1993.

[11] E. C. Hunke. Thickness sensitivities in the CICE sea ice model. *Ocean Modelling*, 34:137–149, 2010.

[12] E. C. Hunke and J. K. Dukowicz. An elastic-viscous-plastic model for sea ice dynamics. *Journal of Physical Oceanography*, 27:1849–1867, 1997.

[13] E. C. Hunke and M. M. Holland. Global atmospheric forcing data for Arctic ice-ocean modeling. *Journal of Geophysical Research*, 112:C04S14, 2007.

[14] E. C. Hunke and W. H. Lipscomb. CICE: the Los Alamos sea ice model documentation and software user's manual version 4.0. Technical report, LANL, 2008.

[15] E. Kalnay, M. Kanamitsu, R. Kistler, W. Collins, D. Deaven, L. Gandin, M Irrendell, S. Saha, G. White, J. Woollen, Y. Zhu, A. Leetmaa, R. Reynolds, M. Chelliah, W. Ebisuzaki, W. Higgins, J. Janowiak, K. C. Mo, C. Ropelewski, J. Wang, R. Jenne, and D. Joseph. The NCEP/NCAR 40-year reanalysis project. *Bull. Amer. Meteor. Soc.*, 77:437–470, 1996.

[16] J. G. Kim, E. C. Hunke, and W. H. Lipscomb. Sensitivity analysis and parameter tuning scheme for global sea-ice modeling. *Ocean Modelling*, 14:61–80, 2006.

[17] R. Kwok, E. C. Hunke, W. Maslowski, D. Menemenlis, and J. Zhang. Variability of sea ice simulations assessed with RGPS kinematics. *Journal of Geophysical Research*, 113:C11012, 2008.

[18] W. G. Large and S. G. Yeager. The global climatology of an interannually varying air-sea flux data set. *Climate Dynamics*, 2008.

[19] W. H. Lipscomb. Remapping the thickness distribution in sea ice models. *Journal of Geophysical Research*, 106:13989–14,000, 2001.

[20] W. H. Lipscomb and E. C. Hunke. Modeling sea ice transport using incremental remapping. *Monthly Weather Review*, 132:1341–1354, 2004.

[21] W. H. Lipscomb, E. C. Hunke, W. Maslowski, and J. Jakacki. Ridging, strength, and stability in high-resolution sea ice models. *Journal of Geophysical Research*, 112:C03S91, 2007.

[22] M. Losch, D. Menemenlis, J. M. Campin, P. Heimbach, and C. Hill. On the formulation of sea-ice models. part 1: Effects of different solver implementations and parameterizations. *Ocean Modelling*, 2010.

[23] G. A. Maykut and N. Untersteiner. Some results from a time-dependent thermodynamic model of sea ice. *Journal of Geophysical Research*, 76(6):1550–1575, 1971.

[24] P. A. Miller, S. W. Laxon, and D. L. Feltham. Consistent and contrasting decadal Arctic sea ice thickness predictions from a highly optimized sea ice model. *Journal of Geophysical Research*, 112(C07020):1–16, 2007.

[25] P. A. Miller, S. W. Laxon, D. L. Feltham, and D. J. Cresswell. Optimization of a sea ice model using basinwide observations of Arctic sea ice thickness, extent, and velocity. *Journal of Climate*, 19:1089–1108, 2006.

[26] C. L. Parkinson and W. M. Washington. A large-scale numerical model of sea ice. *Journal of Geophysical Research*, 84:311–337, 1979.

[27] F. Roske. An atlas of surface fluxes based on the ECMWF reanalysis - a climatolgical dataset to force global ocean general circulation models. Technical report, Max-Planck Institut Fur Meteorologie, 2001.

[28] A. Saltelli, K. Chan, and E. M. Scott. *Sensitivity Analysis*. Wiley Series in Probability and Statistics, New York, 2000.

[29] H. Schreyer, L. Monday, D. Sulsky, M. Coon, and R. Kwok. Elastic-decohesive constitutive model for sea ice. *Journal of Geophysical Research*, 111:C11S26, 2006.

[30] M. C. Serreze, A. P. Barrett, J. C. Stroeve, D. N. Kindig, and M. M. Holland. The emergence of surface-based Arctic amplification. *The Cryosphere*, 3:11–19, 2009.

[31] M. Stein. Large sample properties of simulations using Latin Hypercube Sampling. *Technometrics*, 29(2):143–151, 1987.

[32] J. Stroeve, M. M. Holland, W. Meier, T. Scambos, and M. Serreze. Arctic sea ice decline: Faster than forecast. *Geophysical Research Letters*, 34(L09501):1–5, 2007.

[33] D. Sulsky, Z. Chen, and H. Schreyer. A particle method for history-dependent materials. *Computer Methods in Applied Mechanics and Engineering*, 118:179–196, 1994.

[34] D. Sulsky and K. Peterson. Towards a new model of Arctic sea ice. *Physica D*, submitted, 2010.

[35] D. Sulsky, H. Schreyer, K. Peterson, M. Coon, and R. Kwok. Using the material-point method to model sea ice dynamics. *Journal of Geophysical Research*, 112:C02S90, 2007.

[36] D. Sulsky, S. Zhou, and H. Schreyer. Application of a particle-in-cell method to solid mechanics. *Computer Physics Communications*, 87:236–252, 1995.

[37] A.S. Thorndike, D.A. Rothrock, G.A. Maykut, and R. Colony. The thickness distribution of seaice. *Journal of Geophysical Research*, 80(33):4501–4513, November 1975.

[38] J. Zhang and D. A. Rothrock. Modeling global sea ice with a thickness and enthalpy distribution model in generalized curvilinear coordinates. *Monthly Weather Review*, 131(5):681–697, 2003.

DISTRIBUTION:

1 Elizabeth Hunke
MS-B216
Los Alamos National Laboratory
Los Alamos, NM 87545

2 Deborah Sulsky
Department of Mathematics and Statistics MSC03 2150
1 University of New Mexico
Albuquerque, NM 87131

1	MS 1318	Brian Adams, 1411
1	MS 0828	Ken Alvin, 1544
1	MS 0370	George Backus, 1433
1	MS 9004	Bill Ballard, 8100
1	MS 0370	Mark Boslough, 1433
2	MS 1320	Pavel Bochev, 1414
1	MS 1318	Michael Eldred, 1411
1	MS 1218	Tony Giunta, 5926
1	MS 1322	Oksana Guba, 1433
1	MS 1318	Rob Hoekstra, 1414
1	MS 0321	John Mitchiner, 1430
2	MS 1081	Biliana Paskaleva, 6374
2	MS 1318	Kara Peterson, 1414
1	MS 0828	John Red-Horse, 1544
1	MS 1320	Denis Ridzal, 1411
1	MS 1318	Jim Stewart, 1411
1	MS 0370	Randy Summers, 1433
1	MS 1318	Laura Swiler, 1411
1	MS 0370	Mark Taylor, 1433
1	MS 0899	Technical Library, 9536 (electronic copy)
1	MS 0123	D. Chavez, LDRD Office, 1011

Sandia National Laboratories